

Distributed network interactions and their emergence in developing neocortex

Gordon B. Smith^{1,2,6}, Bettina Hein^{3,4,6}, David E. Whitney^{1,6}, David Fitzpatrick^{ID 1,7*} and Matthias Kaschube^{ID 3,5,7*}

The principles governing the functional organization and development of long-range network interactions in the neocortex remain poorly understood. Using *in vivo* widefield and two-photon calcium imaging of spontaneous activity patterns in mature ferret visual cortex, we find widespread modular correlation patterns that accurately predict the local structure of visually evoked orientation columns several millimeters away. Longitudinal imaging demonstrates that long-range spontaneous correlations are present early in cortical development before the elaboration of horizontal connections and predict mature network structure. Silencing feedforward drive through retinal or thalamic blockade does not eliminate early long-range correlated activity, suggesting a cortical origin. Circuit models containing only local, but heterogeneous, connections are sufficient to generate long-range correlated activity by confining activity patterns to a low-dimensional subspace via multisynaptic short-range interactions. These results suggest that local connections in early cortical circuits can generate structured long-range network correlations that guide the formation of visually evoked distributed functional networks.

The cortical networks that underlie behavior exhibit an orderly functional organization at local and global scales, which is readily evident in the visual cortex of carnivores and primates^{1–6}. Here neighboring columns of neurons represent the full range of stimulus orientations and contribute to distributed networks spanning several millimeters^{2,7–11}. Anatomical studies probing the organization of horizontal connections in visual cortex suggest that network interactions could exhibit considerable functional specificity^{9–11}. However, the fine scale structure of network interactions and the degree to which the activity of a given cortical locus is reliably coupled with the spatiotemporal patterns of activity elsewhere in the network have yet to be determined. Likewise, the sequence of events that leads to the development of mature network interactions is largely unexplored, as these occur at early stages in development when visual stimuli are ineffective in evoking reliable neuronal responses^{12,13}.

Previous studies have suggested that spontaneous activity patterns may be a powerful tool for probing network structure independent of stimulus-imposed organization, one that is applicable especially early in development^{14–18}. This approach is further supported by the finding that under anesthesia, individual spontaneous events can resemble visually evoked activity patterns for stimuli known to engage distributed functional networks^{19,20}.

We therefore sought to exploit the sensitivity and resolution of *in vivo* calcium imaging to probe patterns of spontaneous activity in the mature and developing ferret visual cortex. We first show that in the mature cortex, correlated spontaneous activity exhibits precise local and long-range similarities to modular, orientation selective responses. Employing longitudinal imaging in the developing cortex, we next show that this long-range correlated activity predicts future evoked responses and is generated within intracortical circuits before the emergence of long-range horizontal connectivity.

Lastly, we demonstrate that a circuit model containing only local connections is sufficient to generate long-range correlated activity in close agreement with our empirical data. Together, these results demonstrate that patterns of spontaneous activity recapitulate the precise local and global organization of cortical networks activated by visual stimuli and suggest that large-scale network structure arises early in development through local interactions.

Results

Large-scale modular networks revealed by correlated spontaneous activity. In the awake visual cortex imaged near the time of eye-opening, widefield epifluorescence imaging reveals highly dynamic modular patterns of spontaneous activity that cover millimeters of cortical surface area (Fig. 1a,b and Supplementary Video 1). Spontaneous activity patterns consist of a distributed set of active domains, which become active either near-simultaneously or in a spatiotemporal sequence spreading across the field of view within a few hundred milliseconds.

The strikingly regular modular structure of spontaneous activity patterns suggests a high degree of correlation in the activity of neurons making up this distributed network. To evaluate this correlation structure, we first detected individual large-scale spontaneous events within ongoing spontaneous activity (see Methods), which occurred frequently in the awake cortex (interevent interval: 2.13 s (1.33–6.53 s); duration 1.13 s (0.73–1.73 s); median and interquartile range; $n=5$ animals, Supplementary Fig. 1a,b). The spatial structure of activity was relatively stable, with minor fluctuations over the course of an event, and exhibited frame-to-frame cross-correlations near 0.5 for a 2-s window centered on the peak activity (Supplementary Fig. 2). The frequency and duration of spontaneous events was reminiscent of synchronous states observed in local field potential recordings from awake animals, appearing distinct

¹Department of Functional Architecture and Development of Cerebral Cortex, Max Planck Florida Institute for Neuroscience, Jupiter, FL, USA. ²Optical and Brain Science Medical Discovery Team, Department of Neuroscience, University of Minnesota, Minneapolis, MN, USA. ³Frankfurt Institute for Advanced Studies, Frankfurt, Germany. ⁴International Max Planck Research School for Neural Circuits, Frankfurt, Germany. ⁵Department of Computer Science and Mathematics, Goethe University, Frankfurt, Germany. ⁶These authors contributed equally: Gordon B. Smith, Bettina Hein, David E. Whitney. ⁷These authors jointly directed: David Fitzpatrick, Matthias Kaschube. *e-mail: david.fitzpatrick@mpfi.org; kaschube@fias.uni-frankfurt.de

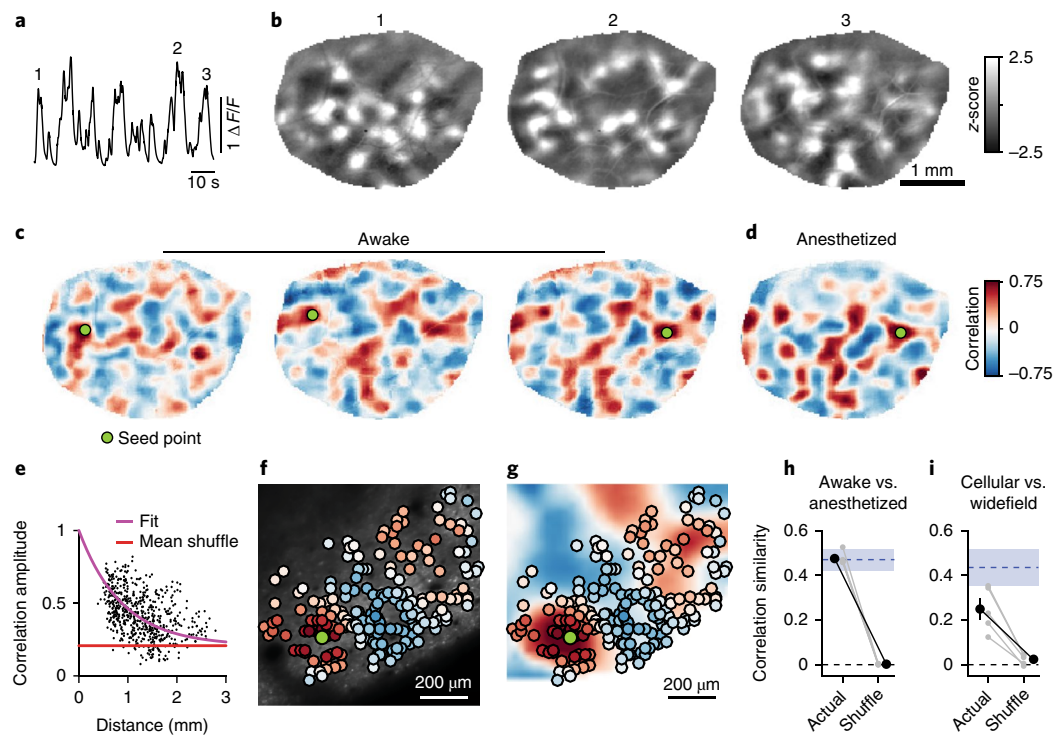


Fig. 1 | Correlated spontaneous activity in awake ferret visual cortex reveals large-scale modular distributed functional networks. **a**, Time-course of spontaneous activity measured with widefield epifluorescence in an awake ferret (mean across pixels in the region of interest (ROI)). **b**, Representative z-scored images of spontaneous events at times indicated by numbers in **a**. **c**, Spontaneous activity correlation patterns (Pearson's correlation) shown for three different seed points (green circle). Correlation patterns span millimeters and can show both rapid changes between nearby seed points (left and middle) and long-range similarity for distant seed points (middle and right). **d**, Correlation patterns are highly similar in the awake and anesthetized cortex. **e**, Correlation values at maxima as a function of distance from the seed point, showing that correlation amplitude remains strong over long distances. **f,g**, Spontaneous activity is modular and correlated at the cellular level (**f**) and shows good correspondence to spontaneous correlations obtained with widefield imaging (**g**). **h**, Correlations measured under anesthesia are statistically similar to those in the awake cortex ($P = 0.031$, one-sided Wilcoxon signed-rank test; $n = 5$; gray, individual animals; black, mean \pm s.e.m.). Blue shaded region indicates within-state similarity (mean \pm s.e.m.). **i**, Cellular correlations are significantly similar to widefield correlations ($P = 0.031$, one-sided Wilcoxon signed-rank test; $n = 5$; gray, individual animals; black, mean \pm s.e.m.). Blue region indicates within-modality similarity (mean \pm s.e.m.).

from both the desynchronized activity often observed during active attention and from the oscillatory activity seen in slow-wave sleep and with certain types of anesthesia²¹.

Spontaneous activity correlation patterns were then computed from detected events by choosing a given seed point and computing its correlation in spontaneous activity with the remaining locations within the field of view. Correlation patterns for a given seed point showed a striking widespread modular organization, with patches of positively correlated activity separated by patches of negatively correlated activity (Fig. 1c). Correlation patterns exhibited significant long-range structure, with statistically significant correlations persisting for more than 2 mm (Fig. 1e; $P < 0.01$ versus surrogate for the example shown, $P < 0.01$ for 10 of 10 animals imaged after eye-opening). The consistency of the correlation patterns was evident in the fact that nearby seed points placed in regions that were negatively correlated exhibit dramatically different spatial correlation patterns (Fig. 1c, left and middle), while seed points placed millimeters away in regions that were positively correlated showed quite similar spatial correlation patterns (Fig. 1c, middle and right). Moving the seed point across the cortical surface revealed a large diversity of correlation patterns (Supplementary Video 2), consistent with principal component analysis revealing that the overall number of relevant global variance components in spontaneous activity patterns was typically larger than ten (Supplementary Fig. 3; 13 ± 3 principal components required to explain 75% variance, mean \pm s.d., $n = 10$).

To determine the impact of brain state and anesthesia on the spatial patterns of correlated spontaneous activity, we followed awake imaging sessions with imaging under light anesthesia (0.5–1% isoflurane). Notably, although spontaneous activity in the awake cortex was more dynamic than under anesthesia, (Supplementary Fig. 4a,c; Supplementary Video 3), the spatial patterns of spontaneous activity, in extent, modularity, and correlation structure, were noticeably similar across states (Fig. 1d,h and Supplementary Fig. 4; $P = 0.031$, one-sided Wilcoxon signed-rank test, $T^+ = 15$, $n = 5$; 5 of 5 experiments from 3 animals individually significant at $P < 0.001$ versus shuffle). Given this strong similarity, awake and anesthetized recordings were pooled in subsequent analyses, and anesthetized recordings were performed exclusively in some experiments.

We next performed two-photon imaging with cellular resolution in conjunction with widefield imaging in the same animal, finding strong and spatially organized spontaneous activity at the cellular level. The duration of events was similar to that observed with widefield imaging (0.88 s (0.54–1.32 s), median and interquartile range), and within an event the pattern of active cells was largely consistent across time (frame-to-frame correlations > 0.5 for 1 s around the peak frame within an event, $P < 0.01$ versus random epochs, bootstrap test). Cellular spontaneous events exhibited similar durations to events detected in widefield data (Supplementary Fig. 1 and Supplementary Video 4). The modular organization of spontaneous activity and the spatial correlation patterns observed in populations of individual layer 2/3 neurons were well-matched to those found

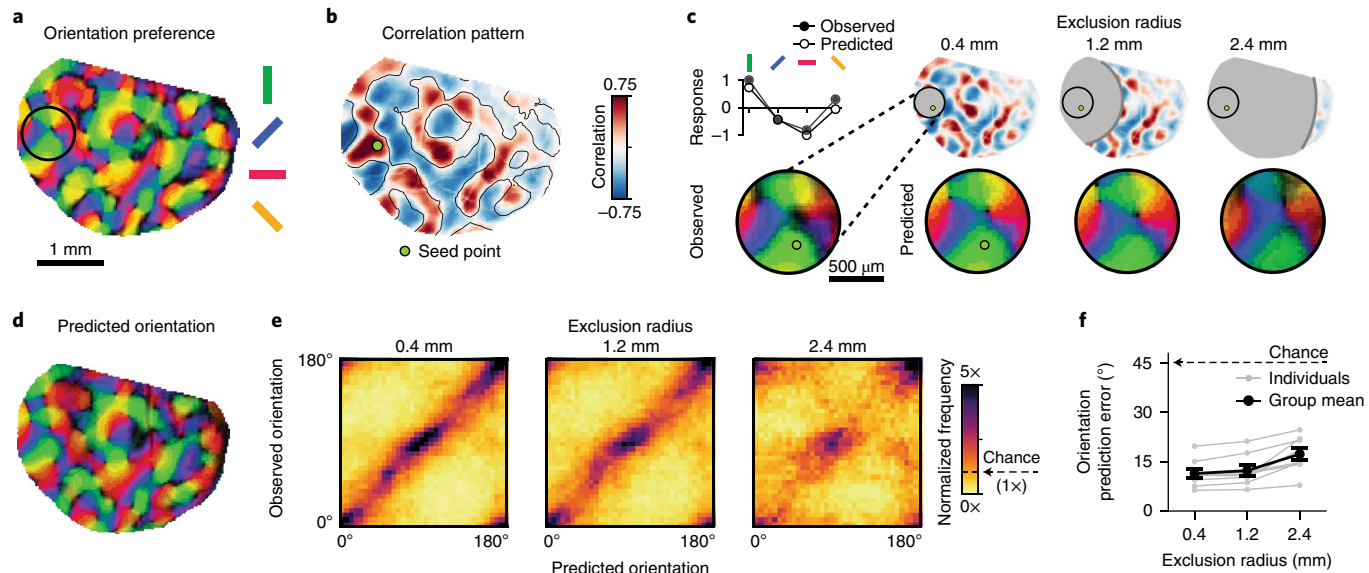


Fig. 2 | Tuning properties can be predicted from correlated network elements several millimeters away. **a**, Orientation preference map. **b**, Spontaneous correlation pattern (Pearson's correlation) for indicated seed point. Contour lines from vertical selective domains from **a** reveal that spontaneous correlations closely resemble the layout of orientation preference map. **c**, Local orientation tuning for region within black circle in **a** can be accurately predicted from the aggregate orientation tuning of distant cortical locations, weighted by long-range correlations. Top left: observed and predicted tuning for the single pixel shown below. Bottom left: observed orientation tuning. Right: accurate orientation predictions based on increasingly distant regions of spontaneous correlations (excluding pixels within 0.4, 1.2, or 2.4 mm from the seed point). **d**, The prediction based on correlations > 1.2 mm away (excluding all correlations < 1.2 mm from seed point) matches the actual preferred orientation within the entire field of view (see **a**). **e**, Across animals, the precision of predicted orientation tuning remains high, even when based on restricted regions more than 2.4 mm away from the site of prediction (see **c**). **f**, Prediction error as function of exclusion radius (45° is chance level). For **e,f**: $n=8$ animal experiments with 5 d or more of visual experience (gray); group data in **f** is shown as mean \pm s.e.m. (black).

with widefield imaging, demonstrating that the network structures revealed with widefield epifluorescence imaging reflected the spatial activity patterns of individual neurons in superficial cortex (Fig. 1f,g,i; $P=0.031$, one-sided Wilcoxon signed-rank test, $T^+=15$, $n=5$; 4 of 5 experiments from 3 animals individually significant at $P<0.05$ versus shuffle). Together these results indicate that neurons in layer 2/3 of visual cortex participate in long-range modular networks whose correlation structure appears robust to changes in brain state.

Long-range correlations reflect fine-scale structure of orientation columns. As individual spontaneous events can resemble patterns of activity evoked by oriented stimuli^{19,20}, we sought to determine whether this correlated spontaneous activity, representing an average over many events and therefore potentially revealing the underlying network architecture, accurately reflects the fine-scale structure of modular networks representing stimulus orientation. We first compared the patterns of spontaneous correlations to the spatial layout of visually evoked orientation domains in animals imaged ≥ 5 d after eye-opening, when orientation selectivity is robust (Fig. 2a). We observed seed points for which the spontaneous correlation pattern closely matched the layout of orientation domains, even at remote distances from the seed point (Fig. 2b and Supplementary Fig. 5; mean similarity of orientation preference versus spontaneous: $r_{OP}=0.42 \pm 0.03$; mean \pm s.e.m.; $n=8$). We also found a significantly weaker but above-chance similarity of spontaneous correlations to the ocular dominance map (Supplementary Fig. 5; mean similarity of orientation domains versus spontaneous: $r_{OD}=0.18 \pm 0.04$; mean \pm s.e.m.; $n=3$; $P<0.0001$ versus surrogate for 3 of 3 animals tested; $P=0.02$, Mann–Whitney test). The strong long-range similarity to orientation preference for certain seed points suggests that the orientation tuning at such seed points can

be predicted from the tuning at remote locations that are correlated in spontaneous activity. To test this idea, we computed the sum over tuning curves at distant locations weighted by their spontaneous correlation with the seed point and compared this prediction to the seed point's actual tuning curve (Fig. 2c). Correlated spontaneous activity predicted the preferred orientation in a small circular patch of radius 0.4 mm with a high level of accuracy. Notably, orientation predictions remained highly accurate even when only considering correlations in regions more than 2.4 mm away from the circle's center point (Fig. 2c–f; $P<0.0001$ versus surrogate for all exclusion radii, with 8 of 8 individual animals significant at $P<0.05$ across all exclusion radii), demonstrating a high degree of long-range fidelity in the structure of spontaneously active networks and those evoked through oriented visual stimuli.

Orientation preference displays pronounced heterogeneity in rate of change across the cortical surface, most notably at pinwheel centers,^{2,7,22} thus a more stringent test of the relation of the spontaneous activity to the fine structure of the orientation map is to ask whether spontaneous correlation patterns exhibit an analogous heterogeneity in their rate of change that correlates with the orientation preference map. Moving the seed point across the cortex shows regions of gradual change in correlation structure, punctuated by abrupt shifts in the large-scale pattern (Supplementary Video 2). By computing the rate of change of the correlation pattern as the seed point was moved (see Methods), we observed peaks of large change over relatively small distances (Fig. 3a,b). A systematic mapping across the cortical surface revealed a set of lines, which we termed 'spontaneous fractures' (Fig. 3c). Moving the seed point across any of these fractures led to strong changes in the global correlation pattern, while correlations changed much less when the seed point was moved within the regions between the fractures. Notably, the layout of spontaneous fractures was stable even when only correlations

with remote locations (> 2.4 mm from seed point) were used to predict the local rate of change (Fig. 3c,f; correlation between fracture patterns for full area versus > 2.4 mm: $r = 0.88 \pm 0.04$, mean \pm s.e.m., $n = 8$). Strikingly, the layout of spontaneous fractures closely followed the heterogeneity in the rate of change in preferred orientation (Fig. 3d), which also formed an intricate network of lines across the cortical surface; often, both appeared in tight register with one another (Fig. 3e; $P = 0.0078$, Wilcoxon signed-rank test, $T^+ = 35$, $n = 8$; 8 of 8 individual animals significant at $P < 0.001$ versus shuffle), as highlighted by the positions of pinwheel centers (Fig. 3c,d). Thus, spontaneous fractures are local manifestations of dramatic large-scale diversity in distributed network structure and emphasize that both the fine- and large-scale organizations of correlated spontaneous activity are precisely matched with the structure of the visually evoked orientation network.

Distributed functional networks exist in the early cortex. Having established that the spontaneous correlation structure faithfully captures key aspects of the distributed networks evoked by visual stimulation, we sought to exploit the correlation structure to gain insights into the nature of these networks at earlier stages of development and determine how they evolve to the mature state. Unexpectedly, even at postnatal day (P) 21, 10 d before eye-opening (and the earliest timepoint examined), we observed robust spontaneous activity that exhibited modular patterns extending for long distances across the cortical surface (Fig. 4a and Supplementary Video 5) and with a temporal structure similar to that found in older animals (Supplementary Fig. 2c–e). Likewise, we found strong correlation patterns that displayed pronounced peaks even several millimeters away from the seed point (Fig. 4b), consistent with electrophysiological recordings²³.

Indeed, the spatial scale of spontaneous correlations changed marginally with age and already, 10 d before eye-opening, it was nearly as large as it was 5 d after eye-opening (Fig. 4d,e; correlation spatial scale: $P = 0.86$, Kruskal–Wallis H test, $\chi^2(3) = 0.78$, $n = 29$; correlation strength at 2 mm: $P < 0.0001$ versus surrogate for all groups; across groups: $P = 0.42$, Kruskal–Wallis H test, $\chi^2(3) = 2.82$, $n = 27$). Moreover, spontaneous fractures were already pronounced at the earliest timepoints, indicating the presence of locally highly organized long-range functional networks in the early cortex (Fig. 4c). These observations were unexpected in light of the limited development of long-range horizontal connections at this early age. Anatomical studies in ferret visual cortex show that layer 2/3 pyramidal cell axons exhibit only about two branch points at P22²⁴, extend only up to 1 mm from the cell body²⁵, and are still lacking spatial clusters of synaptic terminals, which are distributed across several millimeters in the mature cortex²⁶ but only start to become evident at about P26–P27^{25,27}.

Early spontaneous correlations predict mature tuning preference. Our finding that modular activity, long-range correlations, and fractures—all the features that define the modular distributed network—are evident at this early age could suggest that the basic structure of the network may already be similar to its mature state. If so, we should be able to predict the structure of the mature visually evoked network from the spontaneous activity correlation patterns at these early timepoints. To test this possibility, we employed chronic recordings starting as early as P21, 10 d before eye-opening, and mapped all imaging data from each animal onto a common reference frame via an affine transformation, allowing us to track the structure of spontaneous correlations across development (Fig. 5a). We assessed the ability to predict local tuning from remote correlated locations—as in Fig. 2f but now applied across age—to predict the visually evoked orientation map from early spontaneous activity. We found that predictions remained fairly accurate up to 5 d before eye-opening and were above chance

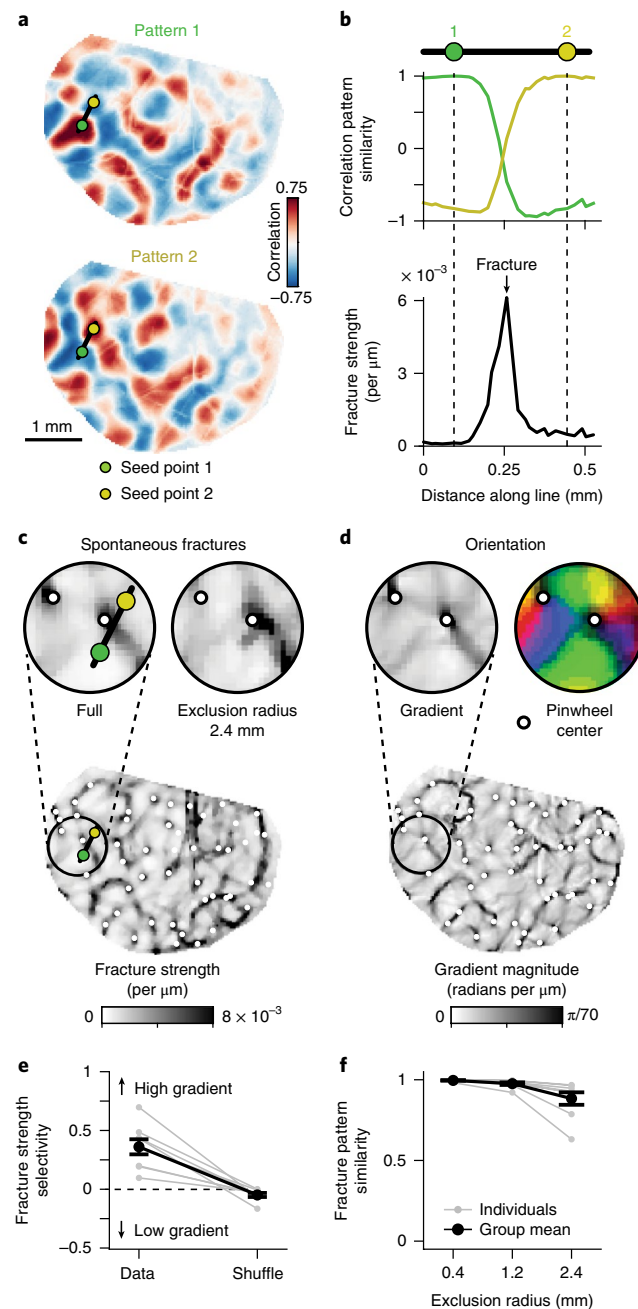


Fig. 3 | Tight relation between global spontaneous correlation and fine-scale structure of orientation columns after eye-opening (EO).

a,b, Fractures in correlated networks. Advancing the seed point along the black line (a) reveals a punctuated rapid transition in global correlation structure, expressed as a high rate of change in the correlation pattern between adjacent pixels (b, bottom). **c,** Locations with high rates of change form a set of lines across the cortical surface, which we termed spontaneous fractures. **d,** The layout of spontaneous fractures precisely coincides with the high-rate-of-change regions in the orientation preference map. **e,** Correlation fractures show selectivity for regions of high orientation gradients. **f,** Fracture location is independent of local correlation structure and remains stable when only long-range correlations are included (see Fig. 2c). For e,f: $n = 8$ animal experiments with 5 d or more of visual experience (gray); group data in e,f is shown as mean \pm s.e.m. (black).

even for the youngest age group, showing that even at this early stage, signatures of the future visually evoked network are apparent (Fig. 5b,c; eye-opening (EO) –10 d to –5 d: $P < 0.0001$ versus

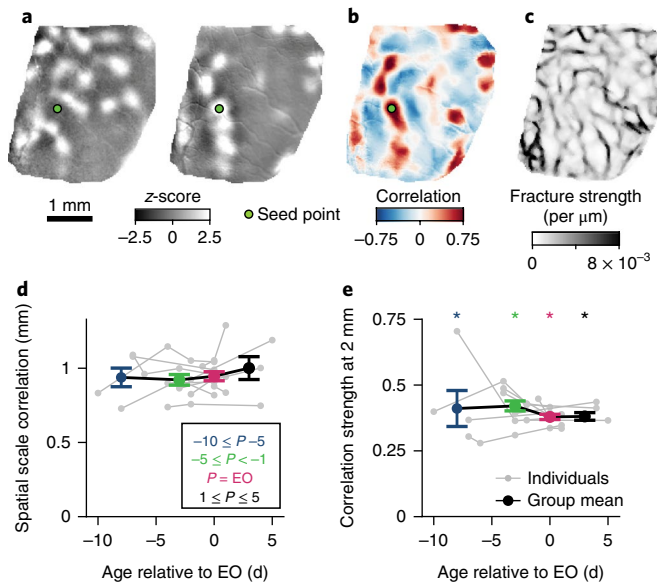


Fig. 4 | Early spontaneous activity exhibits long-range correlations.

a, Representative z-scored images of early spontaneous activity at P23, 7 d before EO. **b,c**, Early spontaneous activity shows hallmarks of mature spontaneous activity, including (**b**) long-range correlated activity (Pearson's correlation) and (**c**) pronounced spontaneous fractures. **d**, The spatial scale of correlations in spontaneous activity (decay constant fit to correlation maxima as function of distance from seed point) is already large early on and changes little across ages. Data points were grouped into four age bins. **e**, The magnitude of long-range correlations for maxima 2 mm from the seed point is statistically significant at all ages examined (* $P < 0.0001$ vs. surrogate data). For **d,e**: $n = 10$ chronically recorded animals; group data is shown as mean \pm s.e.m.

surrogate, 4 of 5 individual data points significant versus surrogate at $P < 0.05$). At the same time, it is clear that there was extensive refinement of the distributed network over this time period (Fig. 5a and Supplementary Fig. 6), such that the ability of the spontaneous correlation patterns to predict the visually evoked orientation patterns increased significantly with age (Fig. 5c; $P = 0.0004$, Kruskal–Wallis H test $\chi^2(3) = 18.08$, $n = 31$; EO –10 d to –5 d vs. EO: $P = 0.004$, Wilcoxon rank-sum test, $U_{10} = 0.0$, $n = 12$). It is also clear that the refinement during this period involved a rearrangement in the spatial organization of spontaneous fractures (Supplementary Fig. 6c,f).

Long-range correlations persist in early cortex despite silencing feedforward drive. Having demonstrated that modular distributed networks are present before the maturation of horizontal connectivity and predict the system of orientation columns in the mature cortex, we next considered the potential circuit mechanisms capable of generating such large-scale distributed networks in the early cortex. Spontaneous retinal waves are a prominent feature of the developing nervous system²⁸ that exhibit highly organized structure and have been shown to propagate into visual cortex²⁹. To assess a potential contribution of retinal waves to activity patterns in the early cortex, we performed intraocular infusions of tetrodotoxin in conjunction with widefield imaging of spontaneous activity in the cortex. Despite completely abolishing light-evoked responses (response amplitude, preinfusion: 0.357 ± 0.061 $\Delta F/F$, postinfusion: 0.023 ± 0.028 $\Delta F/F$, mean \pm s.e.m.; bootstrap test versus baseline: preinactivation: $P < 0.008$, postinactivation: $P = 0.365$, $n = 3$, P22–P25), we continued to observe large-scale spontaneous events, and the spatial correlation structure was significantly more similar

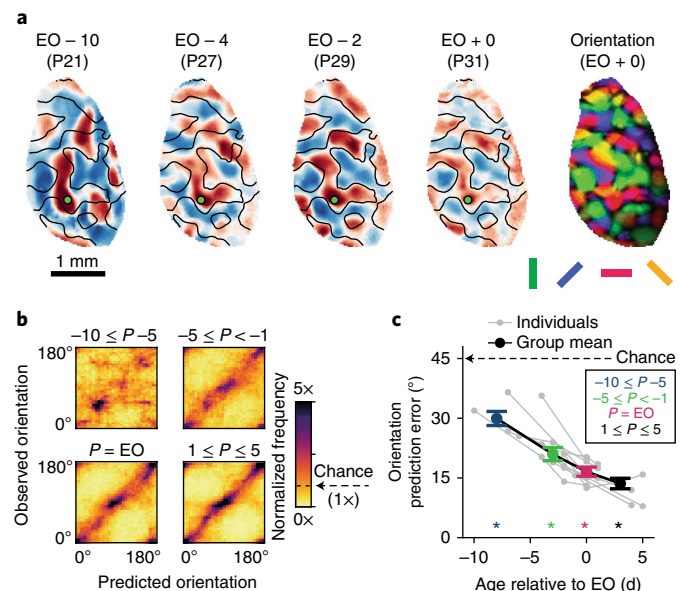


Fig. 5 | Spontaneous activity before EO predicts future evoked responses.

a, Longitudinal imaging of a chronically implanted animal reveals that early spontaneous correlation patterns exhibit signatures of the mature orientation map (right), despite considerable reorganization in correlation structure. Contour lines indicate horizontal selective domains measured at EO. **b**, The structure of spontaneous correlations can predict the future mature orientation preference map organization as early as 10 d before eye opening. **c**, Spontaneous correlation structure predicts orientation preference significantly better than chance, even at the youngest ages examined. * $P < 0.0001$, actual vs. surrogate data; group data is shown as mean \pm s.e.m. For **b,c**: $n = 11$ chronically recorded animals.

to the preinactivation structure than would be expected by chance (Supplementary Fig. 7; similarity versus shuffle, $P < 0.001$ for 3 of 3 animals, bootstrap test).

To address the possibility that coordinated thalamic activity drives large-scale correlations in the early cortex³⁰, we infused muscimol into the lateral geniculate nucleus (LGN) to silence feedforward inputs to the cortex at P22–P25 (Fig. 6a). Muscimol completely blocked light-evoked responses (Fig. 6b; response amplitude, preinfusion: 0.720 ± 0.105 $\Delta F/F$, postinfusion: 0.005 ± 0.006 $\Delta F/F$, mean \pm s.e.m.; bootstrap test versus baseline: preinactivation: $P = 0.0087$, postinactivation: $P = 0.2584$, $n = 3$) and dramatically decreased the frequency of spontaneous events in the cortex (Figs. 6c, < 1 event per min, with a $713 \pm 82\%$ increase in the inter-event interval, mean \pm s.e.m., $n = 3$). However, the events remaining after geniculate inactivation still showed widespread modular activity patterns spanning millimeters and exhibited spatial correlation structures similar to those observed before inactivation (Fig. 6d–f; similarity versus shuffle: $P < 0.001$ for 3 of 3 individual experiments, bootstrap test), consistent with prior experiments in which silencing was induced via optic nerve transection²³. In addition, we found that the spatial layout of correlation fractures was similar following LGN inactivation (fracture similarity: 0.164 ± 0.015 , $P = 0.04$, bootstrap test, $n = 3$ animals), suggesting that the fine-scale structure of correlation patterns was also generated within cortical circuits. Notably, the spatial extent of correlations was unchanged following muscimol (Fig. 6g; control: 1.04 ± 0.12 mm; inactivation: 1.13 ± 0.20 mm, mean \pm s.e.m.), demonstrating that feedforward drive cannot account for the spatial structure and extent of correlated spontaneous activity in the early cortex. These results suggest that the modular, large-scale distributed networks present in

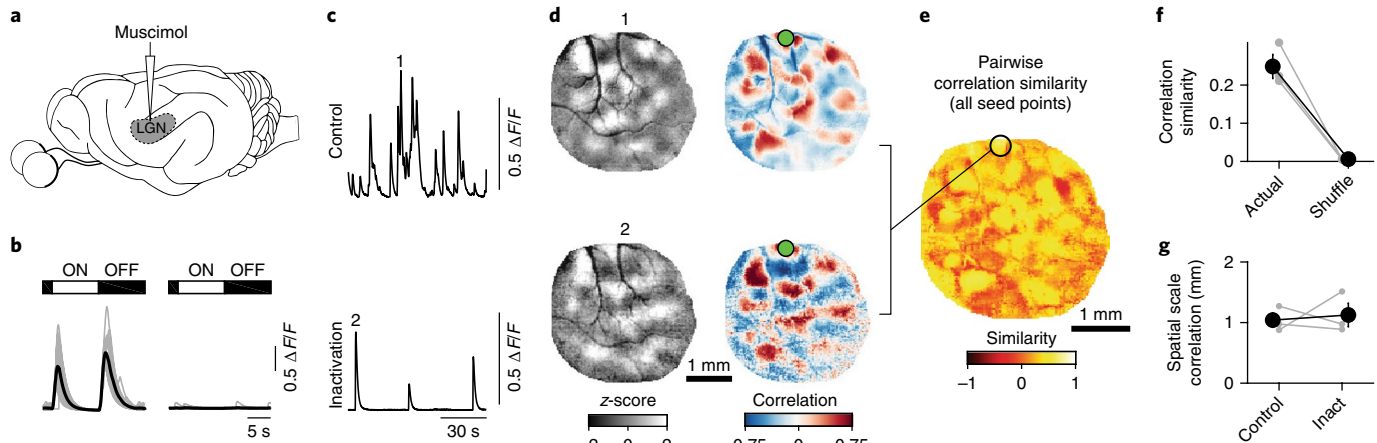


Fig. 6 | Long-range correlations in spontaneous activity persist in the absence of feedforward input. **a**, Cortical spontaneous activity was measured before and following LGN inactivation via targeted muscimol infusion. **b**, Cortical responses (averaged across all pixels in ROI) to full-field luminance changes before (left) and after (right) LGN inactivation. **c**, Time-course of spontaneous activity for mean of all pixels before (top) and after (bottom) inactivation. **d**, Representative spontaneous events (left) and correlation patterns (Pearson's correlation; right) before (top) and after (bottom) inactivation at timepoints indicated by numbers in **c**. **e**, Similarity of correlation structures in representative experiment before and after inactivation for all cortical locations. **f**, Correlation structures were significantly more similar before and after inactivation than shuffled data ($P < 0.001$ vs. shuffle, for 3 of 3 individual experiments, $n = 3$ animals, bootstrap test). Error bars show mean \pm s.e.m. **g**, The spatial scale of spontaneous correlations remains long-range following LGN inactivation ($n = 3$ animals). Error bars show mean \pm s.e.m. Scale bars, 1 mm.

the early visual cortex were intrinsically generated within cortical circuits, rather than being inherited from feedforward pathways.

Heterogeneous circuit models produce large-scale organization from local connections. As large-scale cortical networks are present before the maturation and elaboration of long-range horizontal connectivity, these results also present a conundrum. To explore how a developing cortex lacking long-range connectivity could generate long-range correlated patterns of activity, we examined dynamic network models of firing rate units³¹, variants of which have been used previously to model spontaneous activity in the mature visual cortex^{32–35}. In such models, modular patterns of activity can form via lateral suppression and local facilitation. Such an interaction is often assumed to result from lateral connections that are identical at each position in cortex, circularly symmetric, and follow a 'Mexican-hat' profile^{36,37}. However, despite producing modular patterns of activity, the resulting patterns produced by such connectivity exhibit an unrealistic regular hexagonal structure (Supplementary Fig. 8). Furthermore, due to the symmetries of this connectivity, sampled activity patterns produce correlation patterns that are nearly identical across seed points and decay more rapidly with distance, failing to show long-range structure (Supplementary Fig. 8) and correlation fractures (see below), indicating that this mechanism alone cannot account for the widespread and diverse correlation patterns we observe *in vivo*.

Instead, the rich structural diversity observed in empirical correlation patterns suggests that local network interactions might not be homogeneous across cortex. Moreover, if local connections vary, this may bias the interactions between nearby domains such that some show a stronger tendency to be co-active than others. Such biases can propagate across the network via multisynaptic connections and induce correlations even between remote locations (Fig. 7a). Thus, local but heterogeneous synaptic connections may 'channel' the spread of activity across cortex, potentially explaining the pronounced correlations found between remote network elements.

To test the idea that heterogeneous local connections can produce long-range correlations, we modeled cortical spontaneous activity using a dynamical rate network^{31–35}, in which model units

(representing a local pool of neurons) receive recurrent input from neighboring units weighted by an anisotropic Mexican-hat function whose longer axis varies randomly across the cortical surface (Fig. 7b and see Methods equations (18–20)). To this network we supplied a constant drive, modulated spatially by a Gaussian random field with only local correlations (Fig. 7b and see Methods equation (21)). For sufficiently strong connections, network activity evolves toward a modular pattern with roughly alternating patches of active and nonactive domains (Fig. 7b). In a regime of strongly heterogeneous connectivity and moderate input modulation (referred to as the heterogeneous regime in the following), the model produces pronounced long-range correlations (Fig. 7c,d and Supplementary Fig. 9a,b) and correlation fractures (Fig. 7e and Supplementary Fig. 9c,d), both in quantitative agreement with experimental results (Fig. 7h). The model also suggests that the spatial structure of correlated activity should be fairly robust against changes in input drive strength (see Methods equation (18)), which is consistent with our empirical observations following the inactivation of the retina and LGN (Fig. 6a–g and Supplementary Fig. 7). In contrast, these properties do not match experimental data if lateral connections are homogeneous and isotropic (Fig. 7d,h).

If local network connections are actually heterogeneous across cortex, we wondered whether this would leave a signature on the local structure of correlated activity, rendering the correlation peak around the seed point anisotropic and variable across space. Indeed, fitting an ellipse to the correlation peak in the model and assessing the degree of eccentricity (Supplementary Fig. 9g and see Methods equation (15)) demonstrates a high degree of anisotropy in the local correlation structure. Notably, our experimental data displays a similar degree of eccentricity in the local correlation peaks and closely matches the values observed in the heterogeneous model regime (Fig. 7f and Supplementary Fig. 9g,h).

Moreover, if heterogeneous connections constrain the layout of activity patterns, then some patterns should occur more frequently while others are suppressed^{32,33,38,39}, effectively reducing the dimensionality of the space spanned by the patterns. To test this prediction, we assessed the dimensionality of this activity space in both model and experiment (see Methods, equation (16)). We find that whereas the dimensionality of the input patterns to the model is

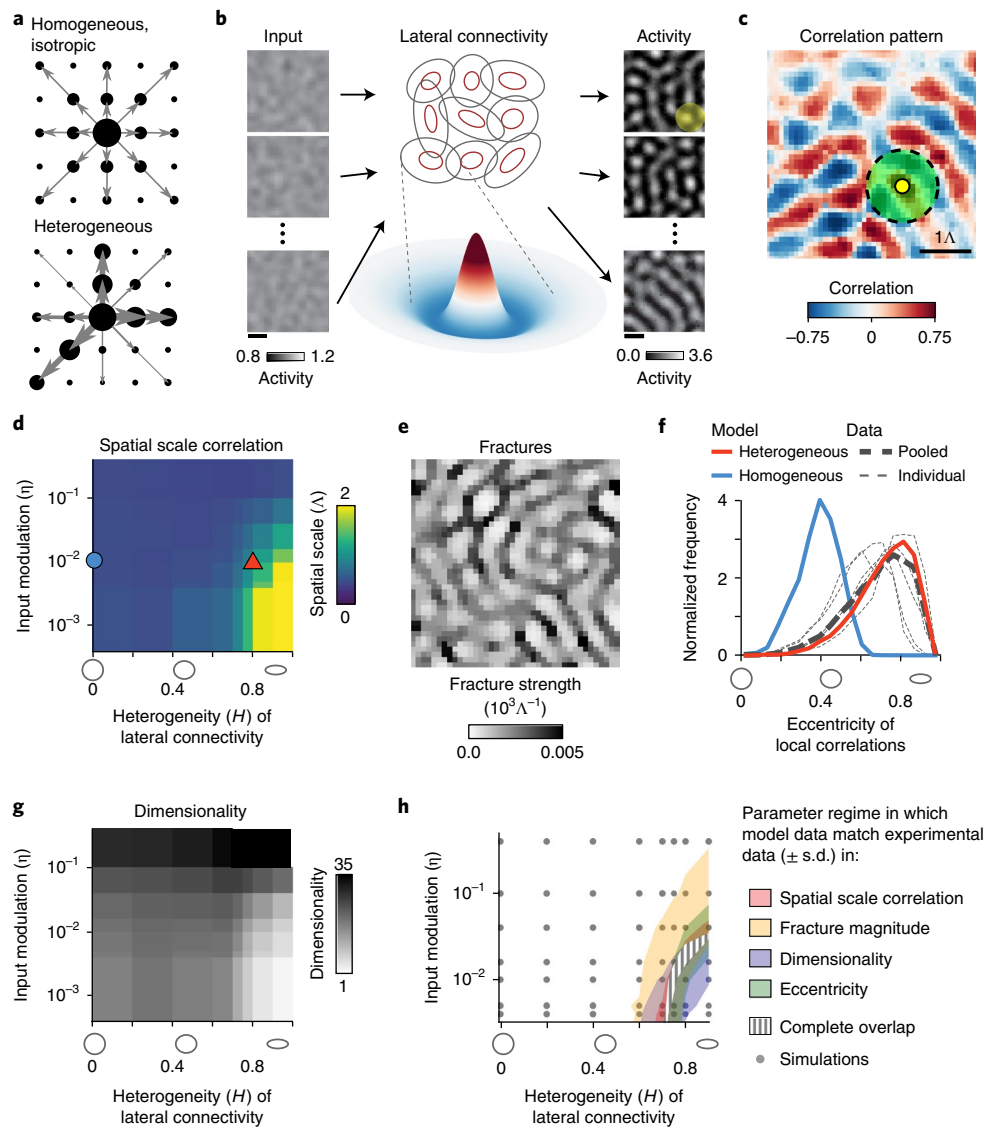


Fig. 7 | Circuit mechanisms for long-range correlations in early visual cortex. **a**, Homogenous local connections (arrows) induce moderate correlations (medium-sized dots) with all nearby domains (black dots), whereas heterogeneity introduces biases, strengthening some correlations (large dots) more than others (small dots). **b**, A dynamical circuit model of spontaneous activity in the early cortex: constant input modulated spatially by filtered noise is fed into a recurrent network with short-range, heterogeneous Mexican-hat (MH) connectivity. It produces a set of modular output patterns with typical spatial scale Λ determined by the MH size (average MH size (2 s.d. of its negative part) illustrated by the yellow circle). **c**, In the heterogeneous regime, the model shows long-range correlations in agreement with experiment (heterogeneity $H = 0.8$; input modulation (s.d. of noise component) $\eta = 0.01$; $n = 100$ output patterns, 16% of modeled region shown; top). **d**, The spatial scale of correlations increases with increasing heterogeneity in the lateral connections and also with decreasing input modulation. Red triangle, the parameters used in **c**; blue circle, isotropic homogeneous connectivity, inconsistent with the range of correlations in experimental data (compare with Fig. 4d and Supplementary Fig. 8). **e**, Pronounced fracture pattern in the heterogeneous regime (same parameters as in **c**). **f**, Match of empirical data to model predictions of local correlation eccentricity (same parameters as in **c**). **g**, The dimensionality of $n = 100$ output patterns produced by the model decreases with increasing heterogeneity and decreasing input modulation. **h**, In the parameter regime in which the model spontaneous patterns approach the empirically observed dimensionality, their short- and long-range correlation structures are in quantitative agreement with experimental data. Shaded regions show parameter regimes in the model in which different properties lie within the range (mean \pm s.d.) of the experimental values (using $1\Lambda = 1\text{mm}$, linear interpolation between simulations). Scale bars, domain spacing 1Λ (**b,c,e**).

high (by construction), the dimensionality of the output patterns in the heterogeneous regime is much smaller and similar to that of experimental data (Fig. 7g,h and Supplementary Fig. 9e,f).

Notably, these results might imply an intimate connection between low-dimensionality, long-range correlations, anisotropic local correlations, and pronounced fractures. To test this idea, we studied the correlation structure in a minimal statistical model of an ensemble of spatially extended modular activity patterns that

are maximally random but confined to a subspace of predefined dimensionality k (Supplementary Fig. 10 and see Methods). Indeed, when the dimensionality is relatively low, this simple statistical model produces not only strong correlations over large distances but also anisotropic local correlations and a network of pronounced correlation fractures (Supplementary Fig. 10c). These results raise the possibility that low dimensionality could be an organizing principle that is sufficient to explain the observed features of correlated

spontaneous activity. This suggests that any mechanism that reduces the dimensionality of spontaneous activity could have similar effects on its correlation structure, including alternative forms of heterogeneity in connectivity or in cellular properties.

So far we have assumed modular activity patterns are generated by Mexican-hat-shaped connectivity. Although there is some evidence for Mexican-hat structures in early ferret visual cortex³⁶, the presence of an anatomical Mexican-hat has yet to be established. To address this, we generated an excitatory–inhibitory two-population model in which the range of lateral excitation exceeds that of inhibition, an arrangement consistent with recordings in mature cortical slices³⁷ (Supplementary Fig. 8 and see Methods equations (22–26)). Consistent with refs^{40,41}, we found that a Mexican-hat is not strictly required for the formation of modular patterns, which can arise even if the range of lateral excitation exceeds that of inhibition (Supplementary Fig. 8). Notably, both the Mexican-hat and the excitatory–inhibitory two-population model show similar increases in the spatial range of correlations as the heterogeneity in the lateral connections is increased (Supplementary Fig. 11), suggesting that the effects of local heterogeneity depend only weakly on the specific form of network interactions generating modular activity. Thus, our computational models describe a plausible mechanism for how the early cortex, even in the absence of long-range horizontal connections, could produce spontaneous activity that is correlated over large distances.

Discussion

Evidence in support of a fundamental modular structure for distributed network interactions in visual cortex has been derived from previous studies documenting the orientation specificity of long-range horizontal connections^{9–11} and in the similarity of spontaneous activity imaged with voltage-sensitive dye to the modular patterns of activity evoked with grating stimuli^{19,20}. Our analysis of spontaneous activity in mature visual cortex extends these observations by showing the remarkable degree of precision that is evident in the correlated activity of long-range network interactions, such that the activity patterns of small populations of neurons accurately predict the structure of local functional architecture over broad regions of cortex covering millimeters of surface area. Even the finest-scale topographic features of orientation maps—the fractures or pinwheel centers—are accurately reflected in the long-range network interactions evident from correlated spontaneous activity. These results, together with the stability of large-scale correlation patterns across awake and anesthetized states, demonstrate an exceptional degree of functional coherence in cortical networks, a coherence that transcends the columnar scale and likely insures reliable distributed neural representations of sensory input.

Patterns of spontaneous activity also allowed us to characterize the state of distributed network structure early in development. Given the strong association of modular activity patterns with the modular arrangement of long-range horizontal connections in mature cortex^{9–11}, we were surprised to find robust long-range modular patterns of correlated activity as early as 10 d before eye-opening, when horizontal connections are immature^{24,25,27}. We emphasize that the correlated patterns of activity at this developmental stage are not identical to the patterns found in the mature cortex; instead they undergo considerable refinement in the period before eye-opening. Indeed, developmental changes in the patterns of correlated activity are likely to reflect ongoing maturation of multiple features of circuit organization, including the emergence of long-range horizontal connections. Nevertheless, the presence of such long-range modular correlation patterns in the absence of a well-developed horizontal network in layer 2/3 challenges the necessity of long-range monosynaptic connections for generating distributed modular network activity^{27,42}.

Furthermore, our retinal and thalamic inactivation experiments bolster previous work²³ and definitively establish that early correlated patterns of spontaneous activity cannot be attributed to patterns of activity arising from retina or LGN. The finding that modular correlation patterns were distributed over distances comparable to those found with intact feedforward inputs indicates that immature cortical circuits have the capacity to generate long-range modular patterns. We emphasize that these observations do not rule out a causal role for feedforward inputs in establishing modular cortical network structure. Patterns of retinal and geniculocortical activity could play a critical role in guiding the development of these cortical activity patterns (for example, refs^{43–45}), but they are clearly not required for their expression.

Together, these results present a challenging puzzle: long-range correlated activity in the early cortex is generated through intracortical circuits in the absence of long-range horizontal connectivity. Our dynamical model suggests a powerful solution by showing that long-range correlations can arise as an emergent property in heterogeneous circuits via multisynaptic short-range interactions that tend to favor certain spatially extended activity patterns at the expense of others. By confining the space of possible large-scale activity patterns to a low-dimensional subspace, long-range order is established in the form of distributed coactive domains, explaining our observation of long-range spontaneous correlations in the early visual cortex. These results also suggest that the high degree of local precision evident in mature distributed network interactions could derive from the origin of network structure in early local interactions that seed the subsequent emergence of clustered long-range horizontal connections via Hebbian plasticity mechanisms.

Online content

Any methods, additional references, Nature Research reporting summaries, source data, statements of data availability and associated accession codes are available at <https://doi.org/10.1038/s41593-018-0247-5>

Received: 7 June 2018; Accepted: 22 August 2018;
Published online: 22 October 2018

References

- Hubel, D. H. & Wiesel, T. N. Receptive fields and functional architecture of monkey striate cortex. *J. Physiol. (Lond.)* **195**, 215–243 (1968).
- Blasdel, G. G. & Salama, G. Voltage-sensitive dyes reveal a modular organization in monkey striate cortex. *Nature* **321**, 579–585 (1986).
- Weliky, M., Bosking, W. H. & Fitzpatrick, D. A systematic map of direction preference in primary visual cortex. *Nature* **379**, 725–728 (1996).
- Issa, N. P., Trepel, C. & Stryker, M. P. Spatial frequency maps in cat visual cortex. *J. Neurosci.* **20**, 8504–8514 (2000).
- Kara, P. & Boyd, J. D. A micro-architecture for binocular disparity and ocular dominance in visual cortex. *Nature* **458**, 627–631 (2009).
- Smith, G. B., Whitney, D. E. & Fitzpatrick, D. Modular representation of luminance polarity in the superficial layers of primary visual cortex. *Neuron* **88**, 805–818 (2015).
- Bonhoeffer, T. & Grinvald, A. Iso-orientation domains in cat visual cortex are arranged in pinwheel-like patterns. *Nature* **353**, 429–431 (1991).
- Ohki, K., Chung, S., Ch'ng, Y. H., Kara, P. & Reid, R. C. Functional imaging with cellular resolution reveals precise micro-architecture in visual cortex. *Nature* **433**, 597–603 (2005).
- Gilbert, C. D. & Wiesel, T. N. Columnar specificity of intrinsic horizontal and corticocortical connections in cat visual cortex. *J. Neurosci.* **9**, 2432–2442 (1989).
- Malach, R., Amir, Y., Harel, M. & Grinvald, A. Relationship between intrinsic connections and functional architecture revealed by optical imaging and *in vivo* targeted biocytin injections in primate striate cortex. *Proc. Natl Acad. Sci.* **90**, 10469–10473 (1993).
- Bosking, W. H., Zhang, Y., Schofield, B. & Fitzpatrick, D. Orientation selectivity and the arrangement of horizontal connections in tree shrew striate cortex. *J. Neurosci.* **17**, 2112–2127 (1997).
- Chapman, B. & Stryker, M. P. Development of orientation selectivity in ferret visual cortex and effects of deprivation. *J. Neurosci.* **13**, 5251–5262 (1993).

13. Chapman, B., Stryker, M. P. & Bonhoeffer, T. Development of orientation preference maps in ferret primary visual cortex. *J. Neurosci.* **16**, 6443–6453 (1996).
14. Smith, S. M. et al. Functional connectomics from resting-state fMRI. *Trends Cogn. Sci.* **17**, 666–682 (2013).
15. Matsui, T., Murakami, T. & Ohki, K. Transient neuronal coactivations embedded in globally propagating waves underlie resting-state functional connectivity. *Proc. Natl Acad. Sci. USA* **113**, 6556–6561 (2016).
16. Carrillo-Reid, L., Miller, J. E., Hamm, J. P., Jackson, J. & Yuste, R. Endogenous sequential cortical activity evoked by visual stimuli. *J. Neurosci.* **35**, 8813–8828 (2015).
17. Luczak, A., Barthó, P. & Harris, K. D. Spontaneous events outline the realm of possible sensory responses in neocortical populations. *Neuron* **62**, 413–425 (2009).
18. Mohajerani, M. H. et al. Spontaneous cortical activity alternates between motifs defined by regional axonal projections. *Nat. Neurosci.* **16**, 1426–1435 (2013).
19. Kenet, T., Bibitchkov, D., Tsodyks, M., Grinvald, A. & Arieli, A. Spontaneously emerging cortical representations of visual attributes. *Nature* **425**, 954–956 (2003).
20. O’Hashi, K. et al. Interhemispheric synchrony of spontaneous cortical states at the cortical column level. *Cereb. Cortex* **28**, 1794–1807 (2018).
21. Harris, K. D. & Thiele, A. Cortical state and attention. *Nat. Rev. Neurosci.* **12**, 509–523 (2011).
22. Ohki, K. et al. Highly ordered arrangement of single neurons in orientation pinwheels. *Nature* **442**, 925–928 (2006).
23. Chiu, C. & Weliky, M. Spontaneous activity in developing ferret visual cortex *in vivo*. *J. Neurosci.* **21**, 8906–8914 (2001).
24. Borrell, V. & Callaway, E. M. Reorganization of exuberant axonal arbors contributes to the development of laminar specificity in ferret visual cortex. *J. Neurosci.* **22**, 6682–6695 (2002).
25. Durack, J. C. & Katz, L. C. Development of horizontal projections in layer 2/3 of ferret visual cortex. *Cereb. Cortex* **6**, 178–183 (1996).
26. White, L. E., Coppola, D. M. & Fitzpatrick, D. The contribution of sensory experience to the maturation of orientation selectivity in ferret visual cortex. *Nature* **411**, 1049–1052 (2001).
27. Ruthazer, E. S. & Stryker, M. P. The role of activity in the development of long-range horizontal connections in area 17 of the ferret. *J. Neurosci.* **16**, 7253–7269 (1996).
28. Arroyo, D. A. & Feller, M. B. Spatiotemporal features of retinal waves instruct the wiring of the visual circuitry. *Front. Neural Circuits* **10**, 54 (2016).
29. Ackman, J. B., Burbridge, T. J. & Crair, M. C. Retinal waves coordinate patterned activity throughout the developing visual system. *Nature* **490**, 219–225 (2012).
30. Yang, J. W. et al. Thalamic network oscillations synchronize ontogenetic columns in the newborn rat barrel cortex. *Cereb. Cortex* **23**, 1299–1316 (2013).
31. Wilson, H. R. & Cowan, J. D. A mathematical theory of the functional dynamics of cortical and thalamic nervous tissue. *Kybernetik* **13**, 55–80 (1973).
32. Goldberg, J. A., Rokni, U. & Sompolinsky, H. Patterns of ongoing activity and the functional architecture of the primary visual cortex. *Neuron* **42**, 489–500 (2004).
33. Blumenfeld, B., Bibitchkov, D. & Tsodyks, M. Neural network model of the primary visual cortex: from functional architecture to lateral connectivity and back. *J. Comput. Neurosci.* **20**, 219–241 (2006).
34. Murphy, B. K. & Miller, K. D. Balanced amplification: a new mechanism of selective amplification of neural activity patterns. *Neuron* **61**, 635–648 (2009).
35. Fernández Galán, R. On how network architecture determines the dominant patterns of spontaneous neural activity. *PLoS ONE* **3**, e2148 (2008).
36. Dalva, M. B. Remodeling of inhibitory synaptic connections in developing ferret visual cortex. *Neural Dev.* **5**, 5 (2010).
37. Levy, R. B. & Reyes, A. D. Spatial profile of excitatory and inhibitory synaptic connectivity in mouse primary auditory cortex. *J. Neurosci.* **32**, 5609–5619 (2012).
38. Renart, A., Song, P. & Wang, X. J. Robust spatial working memory through homeostatic synaptic scaling in heterogeneous cortical networks. *Neuron* **38**, 473–485 (2003).
39. Tsodyks, M. & Sejnowski, T. Associative memory and hippocampal place cells. *Int. J. Neural Syst.* **6**, 81–86 (1995).
40. Ali, R., Harris, J. & Ermentrout, B. Pattern formation in oscillatory media without lateral inhibition. *Phys. Rev. E* **94**, 012412 (2016).
41. Kang, K., Shelley, M. & Sompolinsky, H. Mexican hats and pinwheels in visual cortex. *Proc. Natl Acad. Sci. USA* **100**, 2848–2853 (2003).
42. Shouval, H. Z., Goldberg, D. H., Jones, J. P., Beckerman, M. & Cooper, L. N. Structured long-range connections can provide a scaffold for orientation maps. *J. Neurosci.* **20**, 1119–1128 (2000).
43. Cang, J. et al. Development of precise maps in visual cortex requires patterned spontaneous activity in the retina. *Neuron* **48**, 797–809 (2005).
44. Chapman, B. & Gödecke, I. Cortical cell orientation selectivity fails to develop in the absence of ON-center retinal ganglion cell activity. *J. Neurosci.* **20**, 1922–1930 (2000).
45. Huberman, A. D., Speer, C. M. & Chapman, B. Spontaneous retinal activity mediates development of ocular dominance columns and binocular receptive fields in v1. *Neuron* **52**, 247–254 (2006).

Acknowledgements

We thank D. Ouimet and V. Hoke for technical and surgical assistance, P. Hülsdunk for assistance registering and motion-correcting imaging data, and members of the Fitzpatrick and Kaschube laboratories for helpful discussions. This research was supported by US National Institutes of Health grants EY011488 and EY026273 (D.F.), Bernstein Focus Neurotechnology grant 01GQ0840 (M.K.), BMBF project D-USA-Verbund: SpontVision, FKZ 01GQ1507 (M.K.), the International Max Planck Research School for Neural Circuits in Frankfurt, and the Max Planck Florida Institute for Neuroscience.

Author contributions

All authors designed the study, analyzed the results, and wrote the paper. G.B.S. and D.E.W. performed the widefield and two-photon calcium imaging; B.H. and M.K. performed the computational modeling. G.B.S., B.H., and D.E.W. contributed equally to this work.

Competing interests

The authors declare no competing interests.

Additional information

Supplementary information is available for this paper at <https://doi.org/10.1038/s41593-018-0247-5>.

Reprints and permissions information is available at www.nature.com/reprints.

Correspondence and requests for materials should be addressed to D.F. or M.K.

Publisher’s note: Springer Nature remains neutral with regard to jurisdictional claims in published maps and institutional affiliations.

© The Author(s), under exclusive licence to Springer Nature America, Inc. 2018

Methods

Animals. All experimental procedures were approved by the Max Planck Florida Institute for Neuroscience Institutional Animal Care and Use Committee and were performed in accordance with guidelines from the US National Institutes of Health. We obtained 24 female ferret kits from Marshall Farms and housed them with jills on a 16-h light/8-h dark cycle. See Supplementary Table 1 for complete list of all animals used in each figure. No statistical methods were used to predetermine sample sizes, but our sample sizes are similar to those reported in previous publications (for example, refs 6,13,46).

Viral injections. Viral injections were performed as previously described^{6,46,47}. Briefly we expressed GCaMP6s⁴⁸ by microinjecting AAV2/1.hSyn.GCaMP6s.WPRE.SV40 (obtained from University of Pennsylvania Vector Core) into visual cortex approximately 6–10 d before imaging experiments. Anesthesia was induced with either ketamine (12.5 mg/kg) or isoflurane (4–5%), and maintained with isoflurane (1–2%). Atropine (0.2 mg/kg) and bupivacaine were both administered, and animal temperature was maintained at approximately 37°C with a homeothermic heating blanket. Animals were also mechanically ventilated and both heart rate and end-tidal CO₂ were monitored throughout the surgery. Using aseptic surgical technique, skin and muscle overlying visual cortex were reflected, and a small burr hole was made with a handheld drill (Fordom Electric Co.). Approximately 1 μL of virus contained in a pulled-glass pipette was pressure-injected into the cortex at two depths (~200 μm and 400 μm below the surface) over 20 min using a Nanoject-II (World Precision Instruments). This procedure reliably produced robust and widespread labeling of visual cortex, with GCaMP6 expression typically extending over an area > 3 mm in diameter (Supplementary Fig. 12).

Cranial window surgery. To allow repeated access to the same imaging field, chronic cranial windows were implanted in each animal 0–2 d before the first imaging session. Animals were anesthetized and prepared for surgery as described above. Using aseptic surgical technique, skin and muscle overlying visual cortex were reflected, and a custom-designed metal headplate was implanted over the injected region with MetaBond (Parkell, Inc.). Then both a craniotomy (~5 mm) and a subsequent durotomy were performed, and the underlying brain stabilized with a 1.4 mm thick, 3 mm diameter stacked glass coverslip⁴⁷. The headplate was hermetically sealed with a stainless steel retaining ring (5/16 inch (7.9 mm) internal retaining ring, McMaster-Carr) and glue (VetBond, 3 M). Unless the animal was immediately imaged after a cranial window surgery, the imaging headplate was filled with a silicone polymer (Kwik-kast, World Precision Instruments) to protect it between imaging experiments.

Widefield epifluorescence and two-photon imaging. Widefield epifluorescence imaging was achieved with a Zyla 5.5 sCMOS camera (Andor) controlled by μManager⁴⁹. Images were acquired at 15 Hz with 4 × 4 binning to yield 640 × 540 pixels. Two-photon imaging was performed with a B-Scope microscope (ThorLabs) driven by a Mai-Tai DeepSee laser (Spectra Physics) at 910 nm. The B-Scope microscope was controlled by ScanImage (Vidreo Technologies) in a resonant-galvo configuration with single-plane images (512 × 512 pixels) being collected at 30 Hz.

In animals imaged after eye-opening, phenylephrine (1.25–5%) and tropicamide (0.5%) were applied to the eyes to retract the nictitating membrane and dilate the pupil, and the cornea was protected with regular application of eye drops (Systane Ultra, Alcon Laboratories). The silicon polymer plug overlying the sealed imaging chamber was then gently peeled off. Whenever the imaging quality of the chronic cranial window was found to be suboptimal for imaging, the chamber was opened under aseptic conditions, regrown tissue or neomembrane was removed and a new coverslip was inserted. In some cases, before imaging, animals were paralyzed with either vecuronium or pancuronium bromide (0.2 mg/kg/h in lactated Ringer's, delivered IV).

For imaging experiments in awake animals, animals were habituated to head-fixation beginning at least 2 d before imaging. Habituation consisted of exposure to the fixation apparatus for brief periods, after which animals were returned to their home cage. For imaging, animals were headfixed, and widefield and two-photon imaging was performed as above. For experiments in which both awake and anesthetized imaging were performed, awake imaging was always performed first, followed by anesthesia induction as described above. Awake recordings of spontaneous activity were performed in a darkened room and eye position was not monitored.

For anesthetized longitudinal-imaging experiments, anesthesia was induced with either ketamine (12.5 mg/kg) or isoflurane (4–5%), and atropine (0.2 mg/kg) was administered. Animals were intubated and ventilated, and an IV catheter was placed in the cephalic vein. In some imaging sessions, it was not possible to catheterize the cephalic vein; in these cases, an IP catheter was inserted. Anesthesia was then maintained with isoflurane (0.5–0.75%).

Following imaging, animals were recovered from anesthesia and returned to their home cages. During recovery, neostigmine was occasionally administered to animals that were paralyzed (0.01–0.1 μL/kg per dose).

Visual stimulation. Visual stimuli were delivered on a LCD screen placed approximately 25–30 cm in front of the eyes using PsychoPy⁵⁰. For evoking

orientation responses, stimuli were full-field sinusoidal gratings at 100% contrast, at 0.015–0.06 cycles per degree, drifting at 1 or 4 Hz, and presented at each of eight directions of motion, for 5 s, repeated 8–16 times. In addition, 'blank' stimuli of 0% contrast were also presented. Stimuli were randomly interleaved and were presented for 5 s followed by a 5- to 10-s gray screen. Spontaneous activity was recorded in a darkened room, with the visual stimulus set to a black screen.

Analysis software. Data analysis was performed in Python, ImageJ, and Matlab (MathWorks).

Signal extraction for widefield epifluorescence imaging. To correct for mild brain movement during imaging (especially in the awake state), we registered each imaging frame by maximizing phase correlation to a common reference frame. Furthermore, all imaging experiments acquired during a single day were registered into one reference frame. The ROI was manually drawn around the cortical region with high, robust visually evoked activity. The baseline F_0 for each pixel was obtained by applying a rank-order filter to the raw fluorescence trace with a rank between 15 to 70 and a time-window between 10 and 30 s (values chosen for each imaging session individually, depending on the strength of spontaneous activity). The rank and time window were chosen such that the baseline faithfully followed the slow trend of the fluorescence activity. The baseline corrected spontaneous activity was calculated as $(F - F_0)/F_0 = \Delta F/F_0$.

The baseline for each pixel for the visually evoked activity was obtained by taking the averaged last 1 s of the interstimulus interval immediately before stimulus onset. The grating-evoked response was then calculated as being the average of the fluorescence $\Delta F/F_0$ over the full stimulus period (5 s).

Event detection. To detect spontaneously active events, we first determined active pixels on each frame using a pixel-wise threshold set to 4–5 s.d. above each pixel's mean value across time. Active pixels not part of a contiguous active region of at least 0.01 mm² were considered 'inactive' for the purpose of event detection. Active frames were taken as frames with a spatially extended pattern of activity (> 80% of pixels were active). Consecutive active frames were combined into a single event starting with the first high-activity frame and then either ending with the last high-activity frame or, if present, an activity frame defining a local minimum in the fluorescence activity. To assess the spatial pattern of an event, we extracted the maximally active frame for each event, defined as the frame with the highest activity averaged across the ROI. Notably, calculating the spontaneous correlation patterns (see below) over all frames of all events preserved their spatial structure (Supplementary Fig. 13).

Imaging sessions in which fewer than ten spontaneous events were detected were excluded from further analysis. This threshold was chosen based on randomly sampling (with replacement) a varied number of activity patterns, which revealed that spontaneous correlation patterns (see below) for subsamples of > 10 events were highly similar (second-order correlation ≥ 0.5) to those obtained from all events (Supplementary Fig. 14).

Spontaneous correlation patterns. To assess the spatial correlation structure of spontaneous activity, we applied a Gaussian spatial high-pass filter (with s.d. of Gaussian filter kernel $s_{\text{high}} = 195 \mu\text{m}$) to the maximally active frame in each event and downsampled it to 160 × 135 pixels. The resulting patterns, named spontaneous patterns A in the following, were used to compute the spontaneous correlation patterns as the pairwise Pearson's correlation between all locations \mathbf{x} within the ROI and the seed point \mathbf{s}

$$C(\mathbf{s}, \mathbf{x}) = \frac{1}{N} \sum_{i=1}^N \frac{(A_i(\mathbf{s}) - \langle A(\mathbf{s}) \rangle)(A_i(\mathbf{x}) - \langle A(\mathbf{x}) \rangle)}{\sigma_s \sigma_x} \quad (1)$$

Here the brackets $\langle \rangle$ denote the average over all events and σ_x denotes the s.d. of A over all N events i at location \mathbf{x} . Note that the spatial structure of spontaneous activity was already evident without filtering (Supplementary Fig. 15). High-pass filtering allowed us to extract this spatial structure, but our results did not sensitively depend on the filtering. For instance, weaker high-pass filtering using a kernel with $s_{\text{high}} = 520 \mu\text{m}$ resulted in a highly similar correlation structure (data not shown).

Shuffled control ensemble and surrogate correlation patterns. We compared the real ensemble of spontaneous activity patterns from a given experiment with a control ensemble, obtained by eliminating most of the spatial relationship between the patterns. To this end, all activity patterns were randomly rotated (rotation angle drawn from a uniform distribution between 0° and 360° with a step size of 10°), translated (shifts drawn from a uniform distribution between ± 450 μm in increments of 26 μm, independently for x and y directions) and reflected (with probability 0.5, independently at the x and y axes at the center of the ROI), resulting in an equally large control ensemble with similar statistical properties but little systematic interrelation between patterns. Surrogate correlation patterns were then computed from these ensembles as described above.

Spatial range of correlations. To assess the spatial range of spontaneous correlations (Figs. 1e and 3d), we identified the local maxima (minimum separation between maxima: 800 μm) in the correlation pattern for each seed point and fitted an exponential decay function

$$f(x) = e^{-\frac{x}{\xi}}(1 - c_0) + c_0 \quad (2)$$

to the values of these maxima as a function of distance x to the seed point (Fig. 1e and Supplementary Fig. 9a). Here ξ is the decay constant, named ‘spatial scale correlation’ in Figs. 4d and 7d,h. The baseline c_0 accounts for spurious correlations due to a finite number of spontaneous patterns and was estimated as the average value at maxima 2–3.5 mm away from the seed point in the surrogate correlation patterns described above.

To assess the statistical significance of long-range correlations ~2 mm from the seed point, we compared the median correlation strength for maxima located 1.8–2.2 mm away against a distribution obtained from 100 surrogate correlation patterns. For each individual animal, the P value was taken as the fraction of median correlation strength values from surrogate data greater than or equal to the median correlation strength for real correlation patterns. For 2 of 12 animals, the statistical significance of long-range correlations could not be assessed, due to insufficient coverage in rotated and translated surrogate activity patterns caused by an irregularly shaped ROI. These animals were excluded from analysis of long-range correlation strength.

Comparison of awake and anesthetized correlations. Correlation similarity across awake and anesthetized states was computed for each seed point as the Pearson’s correlation coefficient of the spontaneous correlations for that seed point across states. For each seed point, correlations within 400 μm were excluded from analysis. These ‘second-order correlations’ (shown for each seed point in Supplementary Fig. 4f) were then averaged across all seed points within the ROI. To determine the significance of these second-order correlations across state, we shuffled corresponding seed points across states 1,000 times and again computed correlation similarity. Likewise, to gain an estimate of the expected similarity for a well-matched correlation structure, we computed the similarity of each state to itself. Correlation patterns were first separately computed for half of the detected events, and then the two patterns were compared as above.

Comparison of widefield and cellular correlations. Two-photon images were corrected for in plane motion via a 2D cross-correlation-based approach. For awake imaging, periods of excessive motion were discarded and excluded from further analysis. Cellular ROIs were drawn using custom software (Cell Magic Wand³¹) in ImageJ and imported into Matlab via MIJ (Sage, D., Prodanov, D., Tinevez, J. and Schindelin, J. MIJ: making interoperability between ImageJ and Matlab possible, ImageJ User & Developer Conference, 24–26 October 2012, Luxembourg, <http://bigwww.epfl.ch/sage/soft/mij/>). Fluorescence was averaged over all pixels in the ROI and traces were converted to $\Delta F/F_0^6$, where the baseline fluorescence, F_0 , was computed from a filtered fluorescence trace. The raw fluorescence trace was filtered by applying a 60-s median filter, followed by a first-order Butterworth high-pass filter with a cutoff time of 60 s.

To compute spontaneous correlations (Fig. 1f,g), we first identified frames containing spontaneous events, which were defined as frames in which >30% of imaged neurons exhibited activity >2 s.d. above their mean. The stability of activity during an event was computed as the cross-correlation of each frame with the peak activity frame and was compared to a distribution of 100 randomly chosen intervals of the same length. Cellular activity on all event frames was then z-scored using the mean and s.d. of each frame, and correlation patterns for each cell were computed as the pairwise Pearson’s correlation coefficient using the activity of all neurons on all active frames.

To compare the correlation structure obtained at the cellular level with that obtained via widefield imaging (Fig. 1g) we first aligned the two-photon field of view (FOV) to the widefield image using blood vessel landmarks and applied an affine transformation to obtain the pixel coordinates of each imaged neuron in the widefield frame of reference. Correlation similarity was obtained as above by computing the second-order correlation between the cellular correlation structure and that of the corresponding widefield pixels, using all cells >200 μm from the seed point. Shuffled second-order correlations were obtained by randomly rotating and translating the 2P FOV within the full widefield ROI 1,000 times. To estimate the maximum expected degree of similarity, we computed a second-order correlation within the cellular correlation structure itself by determining the similarity of correlation structures computed using only 50% of detected events (dashed line and blue bar in Fig. 1i).

Orientation preference and ocular dominance maps. The orientation preference maps (Figs. 2a and 5a) were calculated based on the trial-averaged responses evoked by binocularly presented grating stimuli moving in eight directions equally spaced between 0 and 360°. Responses were Gaussian bandpass filtered (s.d.: $s_{low} = 26$ μm, $s_{high} = 195$ μm) and orientation preference was computed by vector summation

$$z(x) = \sum_{k=1}^8 w_k(x) e^{2i\phi_k} \quad (3)$$

with $x = (x, y)^T$

where $w_k(x)$ is the tuning curve at location x , that is, the trial-averaged response to a moving grating with direction ϕ_k at location x . The preferred orientation at x is $0.5 \arg(z(x))$.

Orientation pinwheel centers (Fig. 2i,j) were estimated as described in refs.^{5,23} The Matlab routine provided by Schottorf et al.⁵³ was used. Orientation contour lines (Figs. 2b and 5a) are the zero-levels of the 0–90° difference map, obtained using the matplotlib.pyplot.contours routine. Surrogate orientation-preference maps were obtained by phase-shuffling the original maps in the Fourier domain⁵².

Ocular dominance maps were calculated based on the trial-averaged responses evoked by presenting grating stimuli moving in eight directions equally spaced between 0 and 360° to either the contralateral or ipsilateral eye. The trial-averaged response to each orientation and ocular condition was Gaussian bandpass filtered as described above for the orientation map. Contralateral and ipsilateral response maps were computed by respectively averaging together the trial-average responses to the stimuli presented to the contralateral or ipsilateral eye. The ocular dominance map was computed as the difference of the contralateral and ipsilateral response maps.

Similarity of correlation patterns to the orientation and ocular dominance maps. To quantify how similar patterns of correlated spontaneous activity were to known functional maps in visual cortex, we computed the average pairwise similarity of the spontaneous correlation patterns either to the ocular dominance map or the orientation preference map (Supplementary Fig. 5). The assessment of similarity of each correlation pattern to the ocular dominance map is the magnitude of their pairwise coefficient:

$$r_{OD}(s) = |\text{corr}_x(OD(x), C(s, x))| \quad (4)$$

where $OD(x)$ is the ocular dominance map at location x , $C(s, x)$ is the spontaneous correlation pattern between seed location s and location x , and corr denotes Pearson’s correlation coefficient. Correspondingly, the similarity of each correlation pattern to the orientation map is computed as the magnitude of the pairwise correlation coefficient to the real (Re) and imaginary (Im) components of the vector-summed orientation map z :

$$r_{OP}(s) = \sqrt{\text{corr}_x(\text{Re}(z(x)), C(s, x))^2 + \text{corr}_x(\text{Im}(z(x)), C(s, x))^2} \quad (5)$$

Prediction analysis and exclusion areas. To test whether orientation tuning can be predicted from the tuning at remote locations with correlated spontaneous activity (Fig. 2c), we estimated the tuning curve at seed point $s = (s_x, s_y)$ by the sum over tuning curves w_k at different locations weighted by their spontaneous correlation C with the seed point

$$w_k^{\text{pred}}(s) = \sum_x w_k(x) C(s, x) \quad (6)$$

where k denotes the orientation of the stimulus. The sum was taken over locations x outside a circular area centered on the seed point with radius 0.4, 1.2, or 2.4 mm. For this calculation, both w_k and C are z -scored. To assess the goodness of the prediction, we calculated the angular difference between the predicted and the actual preferred orientation (Fig. 2f). Low values indicate a high match, whereas 45° indicates chance level.

Statistical significance (Fig. 2f) was determined by repeating this analysis for 100 surrogate orientation preference maps, obtained by phase shuffling in the Fourier domain⁵². For individual animals, the P value was taken as the fraction of values equal or smaller than the value for the real orientation map. To pool across animals within an exclusion radius (Fig. 2f), we then generated 10,000 surrogate group medians by randomly drawing from the distributions of surrogate data points (one per animal), and the P value was taken as the fraction of group medians equal to or smaller than the median value for the actual data.

Spontaneous fractures. Fracture strength was defined as the rate by which the correlation pattern changes when changing the seed point location over some small distance (Fig. 3b,c). It was computed as

$$F(s) = \sqrt{F_{dx}(s)^2 + F_{dy}(s)^2} \quad (7)$$

where F_{dx} (or F_{dy}) denotes the x (or y)-component of the rate of change of the correlation pattern at seed point s . We approximated this rate of change by the (second-order) correlation between two correlation patterns with seed points at adjacent pixels a distance d apart

$$F_{dy}(s) = \frac{1 - C_{dy}(s)}{d} \quad (8)$$

$$C_{dy}(s) = \text{corr}_x(C(s, x), C(s + de_y, x)) \quad (9)$$

where corr_x denotes Pearson's correlation coefficient calculated over all locations x and e_y is a unit vector in the y -direction. The subtraction from 1 in the numerator ensures $F=0$ at seed point locations, around which the correlation pattern does not change, while high values of F indicate high changes. We used $d=26\mu\text{m}$, the spatial resolution of the correlation patterns.

We defined fracture magnitude (Supplementary Figs. 9c,d 10f, and 11b) as the difference between F , averaged over the fracture lines, and its average in regions $>130\mu\text{m}$ apart from the nearest fracture line. To extract the fracture lines from F we first applied a spatial median filter with a window size of $78\mu\text{m}$ to remove outliers. We then applied histogram normalization, contrast enhancement using contrast-limited adaptive histogram equalization (CLAHE, clip limit = 20, size of neighborhood $260\times 260\mu\text{m}^2$), and a spatial high-pass filter (Gaussian filter, s.d. $s_{\text{high}}=390\mu\text{m}$). The resulting values were binarized (threshold = 0), and the resulting two-dimensional binary array eroded and then dilated (twice) to remove single noncontiguous pixels. We skeletonized this binary array to obtain the fracture lines.

We quantified the co-alignment between spontaneous fractures and high-orientation-gradient regions by the fracture selectivity (Fig. 3e), defined as the difference between F at high-orientation-gradient locations (x_{high} ; gradient $>\pi/5$ radians/pixel) and locations far from high-orientation gradients (x_{low} ; locations $>150\mu\text{m}$ from x_{high}):

$$FS = \frac{\langle F \rangle_{x_{\text{high}}} - \langle F \rangle_{x_{\text{low}}}}{\langle F \rangle_{x_{\text{high}}} + \langle F \rangle_{x_{\text{low}}}} \quad (10)$$

where the brackets denote average over locations x_{high} and x_{low} respectively. A value of $FS=1$ indicates co-alignment between the spontaneous fractures and the orientation gradient, whereas a value near 0 indicates no such alignment. To assess significance (Fig. 3e) we repeated this analysis for 1,000 surrogate orientation-preference maps, obtained by phase shuffling in the Fourier domain. The P value is the fraction of values equal to or larger than the value for the orientation map.

In order to test whether spontaneous fractures reflect the correlation structure over remote distances and not only in their local neighborhood (Fig. 3c,f), we computed F as above, but excluded a circular region with radius 0.4, 1.2, or 2.4 mm centered at the seed point s . We then computed the Pearson's correlation coefficient with the original F .

Registration for longitudinal imaging. To compare spontaneous correlation patterns across days in longitudinally imaged animals, we transformed all imaging data into a common reference frame (Supplementary Fig. 6a). This transformation corrected for small displacements and expansions of cortical tissue over the imaging period, presumably due to cortical growth. We used an affine transformation, thereby taking into account rotation, scaling, translation, and shear-mapping of the cortex:

$$\mathbf{x}' = T\mathbf{x} + \mathbf{h} \quad (11)$$

$$\text{with } T = \begin{pmatrix} a & b \\ c & d \end{pmatrix} \quad (12)$$

$$\mathbf{h} = (e, f)^T \quad (13)$$

The parameters of the transformation matrix T and of the displacement vector \mathbf{h} were found by minimizing the distance between landmarks determined for each day of experiment. Landmarks were found by marking radial blood vessels (that is, blood vessels oriented orthogonally to the imaging plane) by visual inspection. The following expression was minimized (least square fit) to find transformation parameters from day t to the reference day t_{ref} (eye opening):

$$\sum_{i=1}^N (\mathbf{x}_{t_{\text{ref}},i} - \mathbf{x}'_{t,i})^2 = \sum_{i=1}^N (\mathbf{x}_{t_{\text{ref}},i} - T\mathbf{x}_{t,i} - \mathbf{h})^2 \quad (14)$$

with N landmarks (range: 10–30) in both coordinate systems at coordinates $\mathbf{x}_{t_{\text{ref}},i}$ in the reference coordinate system, and the coordinates $\mathbf{x}_{t,i}$ at day t .

Analysis of spontaneous correlation across development. To compare spontaneous correlation patterns across development, we calculated a second-order correlation (Supplementary Fig. 6d,e) between the correlation patterns on a given day and the reference day (eye opening) with the same seed point. Changes in correlation fractures over development were quantified as the second-order correlation of fracture patterns (Supplementary Fig. 6f). In both cases, an estimate of the expected degree of similarity was computed by first separately computing correlations and their corresponding fracture patterns for half of the detected events, and then computing the second-order correlations as above.

To determine whether correlation patterns early in development can predict mature orientation preferences (Fig. 5c), we computed orientation-tuning predictions as above, using the correlation pattern on a given day to weight tuning curves measured following eye opening, with an exclusion radius of $400\mu\text{m}$. The predicted orientation-preference map was compared to the actual map as described above (see section "Prediction analysis and exclusion areas") for both individual animals and group medians.

To assess the statistical significance of long-range correlation strength at 2 mm across development, we compared correlation maxima to those of surrogate correlation patterns as described above (see section "Spatial range of correlations"). To pool across experiments within an age group, we then generated 10,000 surrogate group medians by randomly drawing from the distributions of surrogate data points (one per experiment), and the P value was taken as the fraction of group medians greater than the median value for the actual data.

Retinal and LGN inactivation experiments. For retinal inactivation experiments, a cranial window was implanted over visual cortex as described above. After imaging spontaneous activity under light isoflurane anesthesia (0.5–1%) as described above, visually evoked responses were recorded in response to full-field luminance steps⁵. Isoflurane levels were then increased and intraocular infusions of TTX were made into each eye. For each intraocular injection, a small incision was made just posterior to the scleral margin using the tip of a 30-gauge needle attached to Hamilton syringe. Each eye was then injected with 2–2.5 μL of 0.75 mM TTX solution (Tocris Bioscience) to reach an intraocular dose of $21.45\mu\text{M}$, roughly comparable to the dosage used previously in ferrets⁵⁴. Following infusion of TTX, isoflurane levels were reduced, and the animal returned to a stable light anesthetic plane. The efficacy of TTX was tested by the absence of visually evoked responses to full-field luminance steps. Following confirmation of retinal blockade, spontaneous activity was imaged as above. Following collection of spontaneous activity, retinal blockade was again confirmed through the absence of cortical responses to visual stimuli.

For LGN inactivation experiments, surgical preparation was as described above. A headpost was implanted near bregma, and a craniotomy was made over visual cortex and sealed with a coverslip affixed directly to the skull with cyanoacrylate glue and dental cement. A second craniotomy was then made over the approximate location of the LGN (Horsley–Clarke coordinates: AP –1 mm, LM +6 mm). The LGN was typically located at a depth of 5–8.5 mm, and its spatial position was mapped by identifying units responsive to a full-field luminance stimulus through systematic electrode penetrations. Once the LGN's position was determined, spontaneous activity in visual cortex was recorded as above, followed by visually evoked responses to luminance steps. A micropipette filled with muscimol (25–100 mM, Tocris Biosciences) was lowered into the center of the LGN, and infusions of $\sim 0.5\mu\text{L}$ were made at three depths along the dorsoventral extent of the penetration using a nanoliter injector (Nanoject). The efficacy of thalamic inactivation was confirmed by the abolishment of visually evoked activity before and after imaging of spontaneous activity in the cortex.

Spontaneous activity was analyzed as described above, with one exception: the ten-event threshold for inclusion (see above) was not applied to the LGN inactivation experiments as, in 1 of 3 cases, fewer than ten events were recorded following LGN inactivation. Comparisons between pre- and postinactivation patterns were made using second-order correlations as described above for comparisons of awake and anesthetized activity.

Local correlation structure. To describe the shape of the peak of a correlation pattern around its seed point (Fig. 7f,g and Supplementary Fig. 9g), we fitted an ellipse (least-square fit) with orientation φ , major axis ς_1 and minor axis ς_2 to the contour line at correlation = 0.7 around the seed point. The eccentricity ϵ of the ellipse is defined as

$$\epsilon = \frac{\sqrt{\varsigma_1^2 - \varsigma_2^2}}{\varsigma_1} \quad (15)$$

Its value is 0 for a circle, with increasing values indicating greater elongation of the ellipse.

Dimensionality of spontaneous activity. We estimated the dimensionality d_{eff} of the subspace spanned by spontaneous activity patterns (Fig. 7 g,h, and Supplementary Figs. 9 e,f,10a) by⁵⁵

$$d_{\text{eff}} = \frac{\left(\sum_{i=1}^N \lambda_i\right)^2}{\sum_{i=1}^N \lambda_i^2} \quad (16)$$

where λ_i are the eigenvalues of the covariance matrix for the N locations (pixels) within the ROI (Supplementary Fig. 9e). These values were compared to the dimensionality of surrogate spontaneous activity patterns by taking the median value of 100 surrogate ensembles generated for each animal as described above (in section "Shuffled control ensemble and surrogate correlation patterns").

Statistical model. To generate a statistical ensemble of spatially extended, modular patterns with predefined dimensionality k (Supplementary Fig. 10), we first synthesized k two-dimensional Gaussian random fields⁵² assuming a power spectrum that is isotropic and has a single Gaussian peak at finite frequency along the radial component with peak frequency and spectral width matched to that of the experimentally observed spontaneous activity patterns (size 100×100 pixels; spatial period $\Lambda_{\text{stat}} = 10$). Interpreting these k patterns as vectors \mathbf{v}_j ($j = 1, \dots, k$) in the high-dimensional pixel space, we orthonormalized them based on a Householder reflection. From these k orthonormal basis vectors \mathbf{v} , we sampled activity patterns A_i ($i = 1, \dots, 10,000$) by linear combinations with coefficients ζ drawn independently from a Gaussian distribution with 0 mean and s.d. equal to 1

$$A_i = \sum_{j=1}^k \zeta_{i,j} \mathbf{v}_j \quad (17)$$

Over this ensemble, we computed the correlation patterns $C(\mathbf{s}, \mathbf{x})$. Note that for finite k even in the limit of infinite samples these patterns generally differ for different seed points \mathbf{s} and their correlation peak values remain finite even at large distance from the seed point (Supplementary Fig. 10d–f). Analogously to the analysis of the experimental data, we computed from the $C(\mathbf{s}, \mathbf{x})$ the fracture strength, anisotropy of local correlations and height of the local maxima at a distance of $2\Lambda_{\text{stat}}$ from the seed point to estimate the strength of long-range correlations (Supplementary Fig. 10c).

Dynamical model. The model addresses the question whether short-range lateral connections can give rise to patterns of spontaneous activity that (i) are modular, (ii) exhibit long-range correlations and (iii) exhibit pronounced spontaneous fractures. Feature (i) can be explained by the Turing mechanism, which for simplicity we implemented by employing Mexican-hat connectivity (local excitation, lateral inhibition), but other network motives can be used as well (see “Model of excitatory and inhibitory neural population” below). The model shows that heterogeneity in the lateral connections is sufficient to explain features (ii) and (iii). Heterogeneity was implemented using elongated Mexican-hats whose properties vary randomly across cortex.

We modeled early spontaneous activity using a two-dimensional firing rate network (Fig. 7) obeying the following dynamics

$$\tau \frac{dr(\mathbf{x}, t)}{dt} = -r(\mathbf{x}, t) + \left[\gamma \sum_y M(\mathbf{x}, \mathbf{y}) r(\mathbf{y}, t) + I(\mathbf{x}) \right]_+ \quad (18)$$

$$[\mathbf{x}]_+ = \begin{cases} \mathbf{x} & \text{if } \mathbf{x} \geq 0 \\ 0 & \text{otherwise} \end{cases} \quad (18A)$$

where $r(\mathbf{x}, t)$ is the average firing rate in a local pool of neurons at location \mathbf{x} , τ is the neuronal time constant, $M(\mathbf{x}, \mathbf{y})$ are the synaptic weights connecting locations \mathbf{x} and \mathbf{y} , $I(\mathbf{x})$ is the input to location \mathbf{x} , and γ is a factor controlling the overall strength of synaptic weights. The connectivity M is assumed to be short-range and to follow a Mexican-hat structure. Moreover, the Mexican-hats are anisotropic, modeled as the difference of two elongated Gaussians, whose axis of elongation and scale vary discontinuously across space

$$M(\mathbf{x}, \mathbf{y}) = \frac{1}{2\pi\sigma_1\sigma_2} \left(\exp\left(-\frac{1}{2}(\mathbf{R}(\mathbf{x}-\mathbf{y}))^T \Sigma^{-1} \mathbf{R}(\mathbf{x}-\mathbf{y})\right) \right)_+ \quad (19)$$

$$\left(-\frac{1}{\kappa^2} \exp\left(-\frac{1}{2\kappa^2}(\mathbf{R}(\mathbf{x}-\mathbf{y}))^T \Sigma^{-1} \mathbf{R}(\mathbf{x}-\mathbf{y})\right) \right)_+$$

$$\text{with } \Sigma = \begin{pmatrix} \sigma_1^2 & 0 \\ 0 & \sigma_2^2 \end{pmatrix} \quad (19A)$$

$$\mathbf{R} = \begin{pmatrix} \cos(\varphi) & -\sin(\varphi) \\ \sin(\varphi) & \cos(\varphi) \end{pmatrix} \quad (19B)$$

Here σ_1 and σ_2 ($\leq \sigma_1$) denote the s.d. values of the smaller Gaussian in the direction of its major and minor axes, respectively. For the larger Gaussian, both s.d. values are scaled by a factor $\kappa > 1$. The level sets of the Gaussians are ellipses whose larger (smaller) axes are proportional to σ_1 (σ_2), and so the eccentricity ϵ (equation (15)) measures the degree of elongation of the Mexican-hat. The angle φ determines the orientation of the elongated Mexican-hat. The dependence of these parameters on cortical space \mathbf{x} is suppressed in equation (20) for brevity. M is normalized such that the magnitude of its maximal eigenvalue is equal to 1. For all simulations we

set $\kappa = 2$, $\tau = 1$, the spatial resolution $\Delta x = 1$, and $\gamma = 1.02$ and used random initial conditions $r(\mathbf{x}, t=0)$ drawn from a uniform distribution between 0 and 0.1.

We introduced the heterogeneity parameter H to parameterize and systematically vary the heterogeneity of elongated Mexican-hats across cortical space \mathbf{x} . The eccentricity ϵ was drawn from a normal distribution with mean $\langle \epsilon \rangle$ and s.d. σ_ϵ , both depending linearly on H ($\langle \epsilon \rangle = H$, $\sigma_\epsilon = 0.13H$). The size of σ_1 was drawn from a normal distribution with s.d. $0.1\langle \sigma_1 \rangle H$ and mean $\langle \sigma_1 \rangle = 1.8$. σ_2 is determined by σ_1 and the eccentricity. The orientation φ of the Mexican-hat axis was drawn from a uniform distribution between 0° and 180° . These three parameters were drawn independently at each location.

In the case of isotropic Mexican-hat connectivity ($\sigma_1 = \sigma_2$) the eigenvectors of M are plane waves, and the spectrum is peaked at the wavenumber $k = 2\pi/\Lambda$; thus the typical spatial scale Λ of the pattern is given by

$$\Lambda^2 = \frac{\pi^2 \sigma_1^2 (k^2 - 1)}{\ln(\kappa)} \quad (20)$$

This defines the spatial scale Λ used as reference in Fig. 7. Inserting the values provided above, $\Lambda \approx 10$. For comparison between model and data we identified 1Λ with 1 mm, which is roughly the spatial scale of spontaneous patterns observed experimentally.

The input drive I is assumed constant in time for simplicity. I is modulated in space using a bandpass-filtered Gaussian random field G with spatial scale Λ , zero mean, and unit s.d.⁵²:

$$I(\mathbf{x}) = 1 + \eta G(\mathbf{x}) \quad (21)$$

We varied the input modulation η between 0.004 and 0.4 in Fig. 4k,l the regime over which we observed a smooth transition from an input-dominated system to a system dominated by the recurrent connections.

To model a spontaneous event, we integrated equation (18) until a near-steady-state of the dynamics was reached. The results in Fig. 7c–h were obtained for an integration time of 500 τ , but a much shorter integration over 50 τ already resulted in similar solutions and nearly the same level of long-range correlations and dimensionality. Different spontaneous events were obtained by using different realizations of input drive I and initial conditions (same connectivity M). To generate Fig. 7d,g,h and Supplementary Figs. 9b,d,f,h and 11 we furthermore averaged over 10 realizations of connectivity M for each parameter setting.

We numerically integrated the dynamics using a fourth-order Runge–Kutta method in a square region of size 100×100 using periodic boundary conditions and a time step $dt = 0.15\tau$. The simulations were performed on the GPUs GeForce GTX TITAN Black and GeForce GTX TITAN X. The code was implemented in Python and Theano (version 0.8.1).

Model of excitatory and inhibitory neural population. To investigate whether modular activity and long-range correlations can be generated without Mexican-hat connectivity, we generated an excitatory/inhibitory two-population model. Building on previous work^{40,41}, the model consists of an excitatory and an inhibitory neural population, and neurons are linked via local lateral connections (with Gaussian profiles). We consider a regime in which the range of connections formed by excitatory neurons is more than 30% larger than that of inhibitory neurons.

Spontaneous activity in the early visual cortex is modeled by the following dynamics

$$\tau \frac{du_e(\mathbf{x}, t)}{dt} = -u_e(\mathbf{x}, t) + \left[\gamma \sum_y (M_{ee}(\mathbf{x}, \mathbf{y}) u_e(\mathbf{y}, t) - M_{ei}(\mathbf{x}, \mathbf{y}) u_i(\mathbf{y}, t)) + J_e(\mathbf{x}) \right]_+ \quad (22)$$

$$\tau \frac{du_i(\mathbf{x}, t)}{dt} = -u_i(\mathbf{x}, t) + \left[\gamma \sum_y (M_{ie}(\mathbf{x}, \mathbf{y}) u_e(\mathbf{y}, t) - M_{ii}(\mathbf{x}, \mathbf{y}) u_i(\mathbf{y}, t)) + J_i(\mathbf{x}) \right]_+ \quad (23)$$

$$[\mathbf{x}]_+ = \begin{cases} \mathbf{x} & \text{if } \mathbf{x} \geq 0 \\ 0 & \text{otherwise} \end{cases} \quad (24)$$

where $u_e(\mathbf{x}, t)$ (or $u_i(\mathbf{x}, t)$) is the average firing rate of an excitatory (or inhibitory) unit at location \mathbf{x} in a two-dimensional model cortex. τ is the neuronal time constant and assumed to be the same for excitatory and inhibitory units. $M_{mn}(\mathbf{x}, \mathbf{y})$ are the synaptic weights connecting location \mathbf{y} in population n to location \mathbf{x} in

population m (where $m, n \in \{e, i\}$, with e being the excitatory and i the inhibitory population). The sum goes over all locations y within the network. γ is a factor controlling the overall strength of synaptic weights. Both excitatory and inhibitory units cover space uniformly and with equal density. $J_m(\mathbf{x})$ is the input to location \mathbf{x} in population m .

The connectivity matrix M consists of the four synaptic weight matrices $M_{mn}(\mathbf{x}, \mathbf{y})$ that are assumed to be short-range and modeled by isotropic Gaussians:

$$M(\mathbf{x}, \mathbf{y}) = \begin{pmatrix} M_{ee}(\mathbf{x}, \mathbf{y}) & -M_{ei}(\mathbf{x}, \mathbf{y}) \\ M_{ie}(\mathbf{x}, \mathbf{y}) & -M_{ii}(\mathbf{x}, \mathbf{y}) \end{pmatrix} \quad (25)$$

$$M_{mn}(\mathbf{x}, \mathbf{y}) = M_{mn}(|\mathbf{x} - \mathbf{y}|) = \frac{a_{mn}}{2\pi\sigma_{mn}^2} \exp\left(-\frac{|\mathbf{x} - \mathbf{y}|^2}{2\sigma_{mn}^2}\right), \quad m, n \in \{e, i\} \quad (26)$$

Here σ_{mn} denotes the s.d. and a_{mn} governs the amplitude of the Gaussian that connects population n to m . The a_{mn} values were normalized such that the maximal eigenvalue of M is equal to 1. Note that the Gaussian connectivity profile is isotropic and identical for all units. Thus, the network connectivity exhibits rotation and translation symmetry.

To model a spontaneous event, we assumed an input drive constant in time and space with a value $J_e(\mathbf{x}) = J_i(\mathbf{x}) = J = 1$. We set $\tau = 1$ and $\gamma = 1.02$ and used random initial conditions $u_e(\mathbf{x}, t=0)$ and $u_i(\mathbf{x}, t=0)$ drawn from a Gaussian distribution with zero mean and unit s.d. rectified at zero. The parameters for the connectivity were set to $a_{ee} = 22.2$, $a_{ie} = a_{ei} = 21.6$, $a_{ii} = 20.8$, $\sigma_{ee} = \sigma_{ii} = 1.9$, $\sigma_{ei} = 1.4$, and $\sigma_{ie} = 0.6$. (Changing these values by 10% produced qualitatively similar results.)

We integrated the network dynamics until a near-steady-state of the dynamics was reached. The results in Supplementary Figs. 8d–h and 11 were obtained for an integration time of 500τ . Different spontaneous events were obtained by using different initial conditions (same connectivity M and input J). We numerically integrated the dynamics using a fourth-order Runge–Kutta method in a square region of size 80×80 using periodic boundary conditions and a time step $d\tau = 0.15\tau$. As above, the simulations were performed on the GPUs GeForce GTX TITAN Black and GeForce GTX TITAN X. The code was implemented in Python and Theano (version 0.8.1).

In our numerical simulations, hexagonal activity patterns occurred for a broad range of connectivity parameters. For specific choices of parameter combinations, we could even obtain this type of solution when setting σ_{ii} to a value similar to σ_{ei} , so that the range of connectivity from inhibition to excitation was similar to that from inhibition to inhibition and when adjusting the strengths a_{ii} and a_{ei} such that the inhibition to excitation was comparable to or slightly stronger than inhibition to inhibition.^{56,57} In other regimes, we also observed uniform or oscillatory solutions.

Notably, the activity patterns produced by this isotropic model reflect the symmetries of the underlying dynamics and thus consist of all translated and rotated versions of a hexagonal pattern, thereby leading to a correlation structure inconsistent with experimental data (Supplementary Figs. 8h and 11b). To address the impact of heterogeneity in the two-population model, we introduce heterogeneity by making the Gaussian connectivity matrices M_{mn} anisotropic and by varying the strength of elongation and the orientation and size of its axis across space (discontinuously, as in the one-population Mexican-hat model):

$$M_{mn}(\mathbf{x}, \mathbf{y}) = \frac{a_{mn}}{2\pi\sigma_{mn}^1\sigma_{mn}^2} \exp\left(-\frac{1}{2}(R(\mathbf{x} - \mathbf{y}))^T \Sigma_{mn}^{-1} R(\mathbf{x} - \mathbf{y})\right) \quad (27)$$

$$\text{with } \Sigma_{mn} = \begin{pmatrix} (\sigma_{mn}^1)^2 & 0 \\ 0 & (\sigma_{mn}^2)^2 \end{pmatrix} \quad (28)$$

$$R = \begin{pmatrix} \cos(\varphi) & -\sin(\varphi) \\ \sin(\varphi) & \cos(\varphi) \end{pmatrix}, \quad m, n \in \{e, i\} \quad (29)$$

Here $M_{mn}(\mathbf{x}, \mathbf{y})$ is the connectivity from location \mathbf{y} in population n to location \mathbf{x} in population m . The quantities σ_{mn}^1 and σ_{mn}^2 denote the s.d. of the Gaussian in the direction of its major and minor axes, respectively. The angle φ determines the orientation of the elongated Gaussian. The dependence of these parameters on cortical space \mathbf{x} is suppressed for clarity.

To systematically study the effect of heterogeneity, we define a heterogeneity parameter H and use eccentricity ε to measure the degree of elongation of the Gaussians, as before (see equation (15)). To construct a network, at each location \mathbf{x} the eccentricity was drawn from a normal distribution with mean $\langle \varepsilon \rangle$ and

s.d. σ_ε , both depending linearly on H ($\langle \varepsilon \rangle = H$, $\sigma_\varepsilon = 0.025H$). The σ_{mn}^1 values were drawn from normal distributions with average values $\sigma_{ee} = \sigma_{ii} = 1.9$, $\sigma_{ei} = 1.4$, and $\sigma_{ie} = 0.6$, respectively, and identical s.d. values equal to $0.003H$. The orientation φ of the Gaussian was drawn from a uniform distribution between 0° and 180° . All parameters were drawn independently at each location \mathbf{x} and were, apart from σ_{mn}^1 , identical for all four Gaussians $M_{mn}(\mathbf{x}, \mathbf{y})$. Finally, each synthesized matrix M was normalized such that the real part of its principle eigenvalue was equal to 1.

To model a spontaneous event, we applied to both the excitatory and the inhibitory population an input drive

$$J_m(\mathbf{x}) = 1 + \eta G_m(\mathbf{x}), \quad m \in \{e, i\} \quad (30)$$

that was constant in time and randomly modulated across space, where G_m is Gaussian white-noise bandpass-filtered around the spatial scale A , which is the dominant scale of activity patterns for the homogeneous isotropic case ($H=0$). The realizations of the Gaussian noise G_m were different for the excitatory and inhibitory populations. Different spontaneous events were obtained by using different realizations of input drive J_m and different initial conditions (same connectivity M). We systematically varied the input modulation strength η between 0.0004 and 0.4. All other parameters and the numerical implementation were identical to the homogeneous isotropic model described above.

Statistical analysis. Nonparametric statistical analyses were used throughout the study. All tests were two-sided unless otherwise noted. Wilcoxon signed-rank, Kruskal–Wallis H -test, and Wilcoxon rank-sum tests were used where indicated above. Bootstrapping and surrogate approaches were used to estimate null distributions for other test statistics as described above. Sample sizes were chosen to be similar to prior studies using similar methodologies in nonmurine species (for example, refs 6,12,13,26,46). All animals in each experiment were treated equivalently, and no randomization or blinding was performed.

Reporting Summary. Further information on research design is available in the Nature Research Reporting Summary linked to this article.

Code availability. The code for data analysis and simulations can be made available upon request to the corresponding author.

Data availability

The data that support the findings of this study are available from the corresponding author upon reasonable request.

References

46. Smith, G. B. et al. The development of cortical circuits for motion discrimination. *Nat. Neurosci.* **18**, 252–261 (2015).
47. Smith, G. B. & Fitzpatrick, D. Viral injection and cranial window implantation for in vivo two-photon imaging. *Methods Mol. Biol.* **1474**, 171–185 (2016).
48. Chen, T. W. et al. Ultrasensitive fluorescent proteins for imaging neuronal activity. *Nature* **499**, 295–300 (2013).
49. Edelstein, A., Amodaj, N., Hoover, K., Vale, R. & Stuurman, N. Computer control of microscopes using μManager. *Curr. Protoc. Mol. Biol.* **Chapter 14**, 20 (2010).
50. Peirce, J. W. PsychoPy—psychophysics software in Python. *J. Neurosci. Methods* **162**, 8–13 (2007).
51. Wilson, D. E. et al. GABAergic neurons in ferret visual cortex participate in functionally specific networks. *Neuron* **93**, 1058–1065.e4 (2017).
52. Kaschube, M. et al. Universality in the evolution of orientation columns in the visual cortex. *Science* **330**, 1113–1116 (2010).
53. Schottendorf, M., Keil, W., Coppola, D., White, L. E. & Wolf, F. Random wiring, ganglion cell mosaics, and the functional architecture of the visual cortex. *PLoS Comput. Biol.* **11**, e1004602 (2015).
54. Cramer, K. S. & Sur, M. Blockade of afferent impulse activity disrupts on/off sublamination in the ferret lateral geniculate nucleus. *Brain. Res. Dev. Brain Res.* **98**, 287–290 (1997).
55. Abbott, L. F., Rajan, K. & Sompolinsky, H. in *The Dynamic Brain: an Exploration of Neuronal Variability and Its Functional Significance* (Ding, M. & Glanzman, D. eds.) Ch. 4, 65–82 (Oxford University Press, Oxford, UK, 2011).
56. Pfeffer, C. K., Xue, M., He, M., Huang, Z. J. & Scanziani, M. Inhibition of inhibition in visual cortex: the logic of connections between molecularly distinct interneurons. *Nat. Neurosci.* **16**, 1068–1076 (2013).
57. Somogyi, P., Kisvárday, Z. F., Martin, K. A. & Whitteridge, D. Synaptic connections of morphologically identified and physiologically characterized large basket cells in the striate cortex of cat. *Neuroscience* **10**, 261–294 (1983).

Reporting Summary

Nature Research wishes to improve the reproducibility of the work that we publish. This form provides structure for consistency and transparency in reporting. For further information on Nature Research policies, see [Authors & Referees](#) and the [Editorial Policy Checklist](#).

Statistical parameters

When statistical analyses are reported, confirm that the following items are present in the relevant location (e.g. figure legend, table legend, main text, or Methods section).

n/a Confirmed

- The exact sample size (n) for each experimental group/condition, given as a discrete number and unit of measurement
- An indication of whether measurements were taken from distinct samples or whether the same sample was measured repeatedly
- The statistical test(s) used AND whether they are one- or two-sided
Only common tests should be described solely by name; describe more complex techniques in the Methods section.
- A description of all covariates tested
- A description of any assumptions or corrections, such as tests of normality and adjustment for multiple comparisons
- A full description of the statistics including central tendency (e.g. means) or other basic estimates (e.g. regression coefficient) AND variation (e.g. standard deviation) or associated estimates of uncertainty (e.g. confidence intervals)
- For null hypothesis testing, the test statistic (e.g. F , t , r) with confidence intervals, effect sizes, degrees of freedom and P value noted
Give P values as exact values whenever suitable.
- For Bayesian analysis, information on the choice of priors and Markov chain Monte Carlo settings
- For hierarchical and complex designs, identification of the appropriate level for tests and full reporting of outcomes
- Estimates of effect sizes (e.g. Cohen's d , Pearson's r), indicating how they were calculated
- Clearly defined error bars
State explicitly what error bars represent (e.g. SD, SE, CI)

Our web collection on [statistics for biologists](#) may be useful.

Software and code

Policy information about [availability of computer code](#)

Data collection

Code and software for data collection is fully described in the methods section of the manuscript. In brief, the following commercial or open source software was used: Micromanager version: 1.4.16; ScanImage version 4.2, MATLAB versions 8.1-9.1; Psychopy version 1.85; ImageJ version 1.51n; MJ version 1.3.9; Cell Magic Wand version 1.0. The code for custom visual stimuli can be made available upon request to the corresponding author.

Data analysis

Custom MATLAB and Python code was used for data analysis and simulations and is described in detail in Methods. In addition to the software listed above, the following commercial and open source software was used: Python versions 2.7, 3; Matplotlib version 2.0.2; Theano version 0.8.1. The following Code availability statement is contained in the manuscript: The code for data analysis and simulations can be made available upon request to the corresponding author.

For manuscripts utilizing custom algorithms or software that are central to the research but not yet described in published literature, software must be made available to editors/reviewers upon request. We strongly encourage code deposition in a community repository (e.g. GitHub). See the Nature Research [guidelines for submitting code & software](#) for further information.

Data

Policy information about [availability of data](#)

All manuscripts must include a [data availability statement](#). This statement should provide the following information, where applicable:

- Accession codes, unique identifiers, or web links for publicly available datasets
- A list of figures that have associated raw data
- A description of any restrictions on data availability

The data that support the findings of this study are available from the corresponding author upon reasonable request.

Field-specific reporting

Please select the best fit for your research. If you are not sure, read the appropriate sections before making your selection.

Life sciences Behavioural & social sciences Ecological, evolutionary & environmental sciences

For a reference copy of the document with all sections, see nature.com/authors/policies/ReportingSummary-flat.pdf

Life sciences study design

All studies must disclose on these points even when the disclosure is negative.

Sample size	No a priori sample size calculations were preformed. 5 animals or greater is an accepted sample size for in vivo imaging in carnivores such as ferrets and cats.
Data exclusions	Data were excluded as noted in methods. In brief, animals with labeled areas insufficiently large to permit correlation scale measurements (2 of 12) were excluded from the analysis of scale.
Replication	All attempts at replication were successful, and all imaged animals are reflected in the data (except as noted above).
Randomization	All comparisons were made within an experimental group (e.g. animals imaged 5+ days after eye opening, longitudinally imaged animals, LGN inactivation animals, etc.), and animals were allocated to an experimental group sequentially, in the order in which experiments were performed
Blinding	No attempts at blinding were performed in this study, as it is not possible to remain blind to animal age or eye opening status. Nor is it possible to remain blind to the pre- or post- inactivation status for retinal or LGN inactivation experiments.

Reporting for specific materials, systems and methods

Materials & experimental systems

n/a	Involved in the study
<input checked="" type="checkbox"/>	<input type="checkbox"/> Unique biological materials
<input checked="" type="checkbox"/>	<input type="checkbox"/> Antibodies
<input checked="" type="checkbox"/>	<input type="checkbox"/> Eukaryotic cell lines
<input checked="" type="checkbox"/>	<input type="checkbox"/> Palaeontology
<input type="checkbox"/>	<input checked="" type="checkbox"/> Animals and other organisms
<input checked="" type="checkbox"/>	<input type="checkbox"/> Human research participants

Methods

n/a	Involved in the study
<input checked="" type="checkbox"/>	<input type="checkbox"/> ChIP-seq
<input checked="" type="checkbox"/>	<input type="checkbox"/> Flow cytometry
<input checked="" type="checkbox"/>	<input type="checkbox"/> MRI-based neuroimaging

Animals and other organisms

Policy information about [studies involving animals; ARRIVE guidelines](#) recommended for reporting animal research

Laboratory animals	Female ferrets age P21-47 were used in this study.
Wild animals	No wild animals were used.
Field-collected samples	No field-collected samples were used.